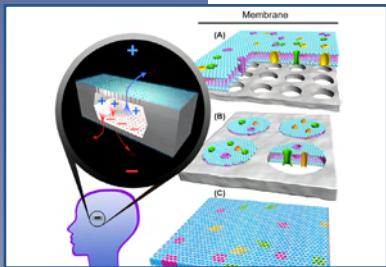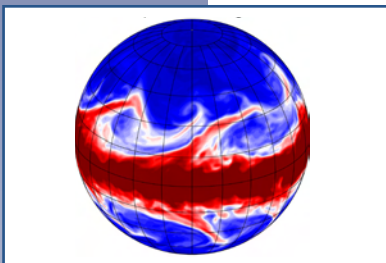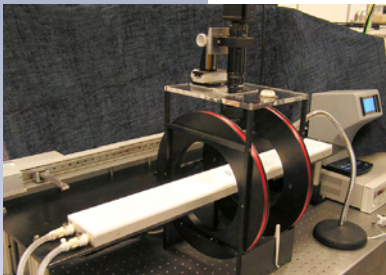# SANDIA NATIONAL LABORATORIES
Science, Technology and Engineering

Bioscience
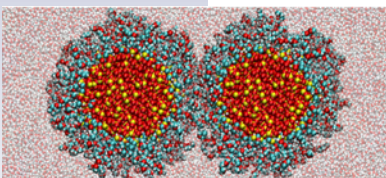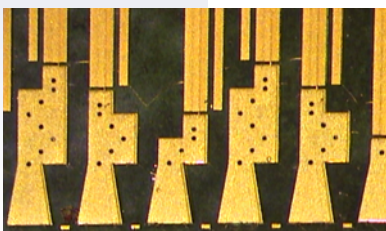
Computers and Information Sciences

Engineering Sciences

Materials Science and Technology

Microelectronics and Microsystems

Pulsed Power

Vision
Sandia National Laboratories is the provider of innovative, science-based, systems-engineering solutions to our Nation's most challenging national security problems.

Mission
Committed to "science with the mission in mind," Sandia creates innovative, science-based, systems-engineering solutions that

- sustain, modernize, and protect our nuclear arsenal,
- prevent the spread of weapons of mass destruction,
- provide new capabilities for national defense,
- defend against terrorism,
- protect our national infrastructures, and
- ensure stable sources of energy and other critical resources.

Guiding principles for ST&E

- Ensure that the fundamental science and engineering core is vibrant and pushing the forefront of knowledge
- Enable the programs by effective application of that science base
    - responding to current needs
    - anticipating the future

About *Science Matters!*
The purpose of *Science Matters!* is to publicize and celebrate recent Sandia accomplishments in science, technology, and engineering. We feature the science that underpins and enables technology for Sandia's missions. We nurture expertise, facilities and equipment to create world-class science that pushes the frontiers of knowledge and anticipates future mission needs. New *Science Matters!* are being issued semiannually.

Sandia National Laboratories

NNSA National Nuclear Security Administration

Cognitive Science and Technology
Neuroscience

Quantum Dots Enable Detection of Neuron Activation

Figure 1: Formation of water-soluble and biocompatible QD-micelles through an interfacially driven micro-emulsion process.

Surfactants/lipids — *or*

Stabilizing organic ligands
Semiconductor QDs
Surfactant/lipids
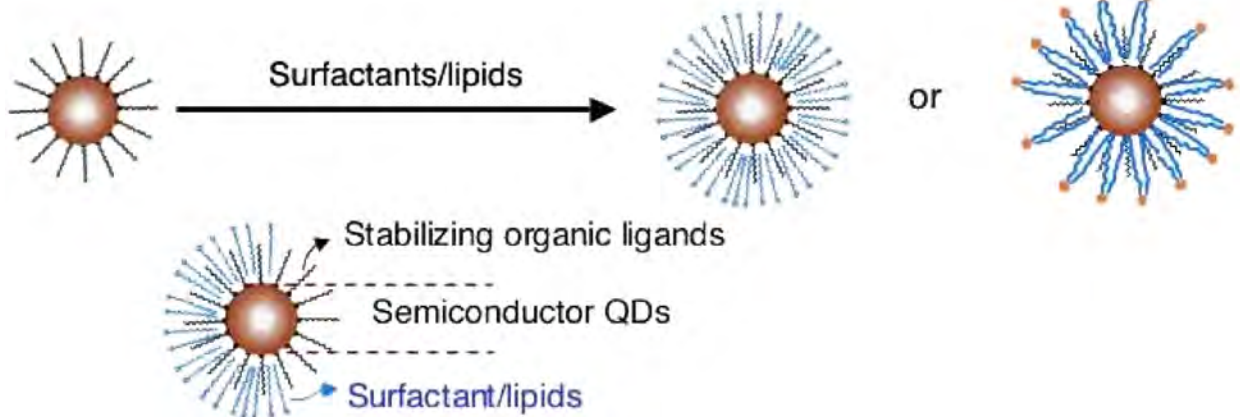
Bioprobes sensitive to membrane potential

For more information:
Technical Contacts:
Hongyou Fan
505-272-7336
hfan@sandia.gov

Chris Forsythe
505-844-5720
jcforsy@sandia.gov

Science Matters Contact:
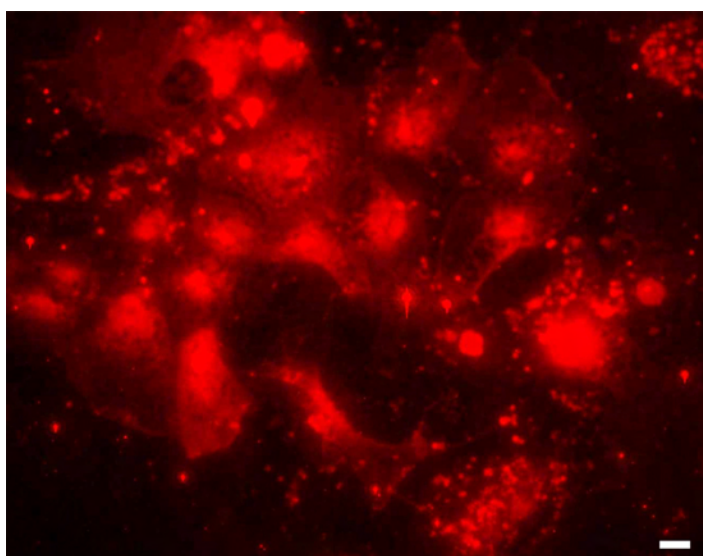Alan Burns, Ph.D
505-844-9642
aburns@sandia.gov

Key processes underlying the operation of individual neurons occur through the binding of neurotransmitter molecules with membrane receptors. Progress in understanding these phenomena requires biocompatible probes that detect neuronal processes within living animals (i.e. *in vivo*). Research conducted through Sandia's Cognitive Science and Technology Initiative has successfully demonstrated that quantum dots (QDs) may be produced that allow fluorescence detection of neuronal voltage changes, and thus exhibit biocompatibility sufficient for their *in vivo* use for many behavioral neuroscience experiments. QDs are generally excellent for fluorescence labeling since they are very bright and stable in comparison with conventional organic dyes.

Monodisperse CdSe and CdSe/CdS core/shell QDs were synthesized through a "hot soap" injection process [1]. Phospholipids were used to encapsulate the QDs within a micelle core to form water-soluble and biocompatible QD micelles (Fig. 1) using an interfacially

driven micro-emulsion process developed at Sandia [2,3]. The interdigitated surfactant layers surrounding the QDs resemble a bilayer structure that enable easy fusion of QDs into cell membranes. In this procedure, a concentrated suspension of QDs in chloroform is added to an aqueous solution containing a mixture of surfactants or phospholipids with different functional head groups such as ethylene glycol (-PEG) and amine (-NH$_2$). PEG is used to improve biocompatibility and amine groups provide sites for bioconjugation. Optical characterization of these biocompatible QD micelles indicated they maintained all the optical properies of the original hydrophobic QDs.

Sensing neuronal potential changes cross-membrane is based on the fluorescent intensity changes of those QDs that are close to or within neuronal membranes. Polarization of the local electric field across the neuronal membrane causes electron/hole pairs to be redistributed within each QD, resulting in an increase in fluorescence as detected by fluorescence imaging. Initial

cell experiments using the QD treated cultured neurons showed a factor of 7 increase in fluorescence intensity in response to this membrane depolarization (Figure 3).

This research demonstrates the use of QDs to detect neuronal voltage changes. QDs have distinct advantages over traditional voltage-indicating fluorescent dyes including high quantum yield and photostability. Further advances should provide the basis for larger scale measurement techniques (e.g., nanoelectrode arrays) essential to gaining an understanding of how nanoscale neural processes aggregate to produce phenomena at the micro (neuron-to-neuron interactions) and millimeter scales (neuronal network interactions).

References:

1. Fan H., et al. *Chem Commun*, *12,* 1383-1394, 2008.
2. Fan, H., et al., *Nano Letters vol. 5*, 645-648, 2005
3. Fan, H., et al., *Science vol. 304*, 567-571, 2004.

Figure 2: Fluorescence image of cultured hippocampal neurons from mouse brain exposed t QDs (590 nm emission). Scale bar =10 μm.

tests utilizing a QD micelle buffer solution to cultured hippocampal pyramidal neurons demonstrated that the micelle bilayer structure promotes the adherence of nanoparticles to the lipid membrane of the neuron with QDs actually becoming wedged within the membrane (Figure 2). The biocompatibility of these QDs ensures the cells to be alive during measurements. The next step was to evaluate whether the quantum dots were sufficiently inserted into the membrane such that they would respond to a change in membrane voltage.

The resting membrane potential of hippocampal pyramidal neurons is largely determined by the equilibrium potential for K^+ and is typically –75 mV. From the Nernst Equation, adding 40 mM KCl to the solution bathing the neurons should change the membrane potential of the cell from –75mV to approximately –21 mV. Live

Figure 3: Fluorescence intensity trace of cultured neurons exposed to 590 nm QDs in a flow chamber of the imaging system. A region of interest was picked over a cell body, the average intensity was calculated, then baseline fluorescence was subtracted. The fluorescence intensity was recorded at 15 s time intervals. The fluorescence was allowed to stabilize in normal artificial cerebrospinal fluid (ACSF) for sample numbers 1-30, then 40 mM KCl was applied to the neurons between sample number 30-60, then washed with normal ACSF for sample numbers 60-100 (bar shows application of KCl)

08/2008
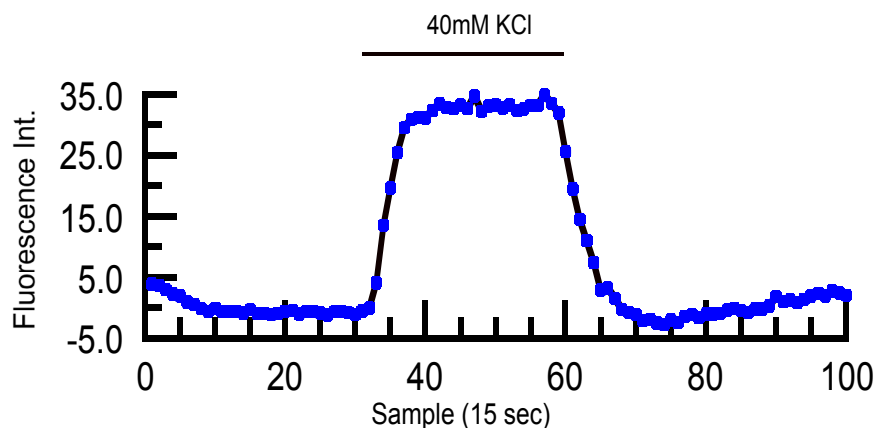
Computers and Information Sciences
Computational Shock and Multiphysics

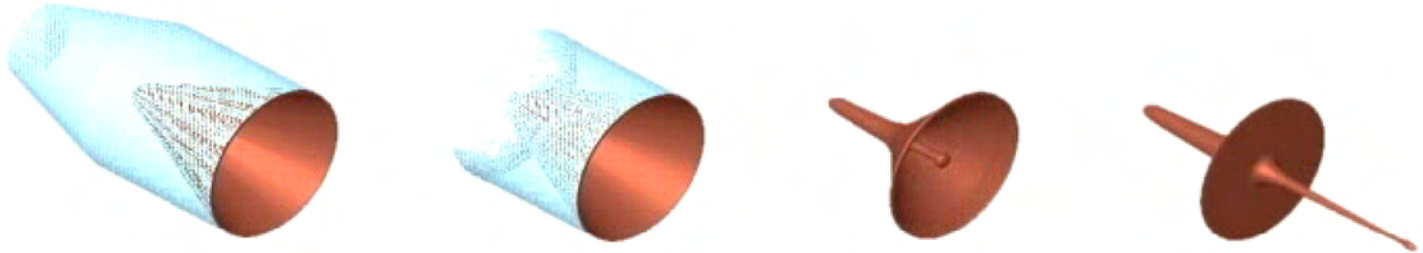# The Power of Simulation: *Unraveling the Mysteries of Electromagnetic Armor*

Figure 1: Formation of a shaped charge jet — Explosive (transparent blue) creates a jet of material as it squeezes a cone-shaped copper liner. (Courtesy Dr. Paul Berning, ARL)
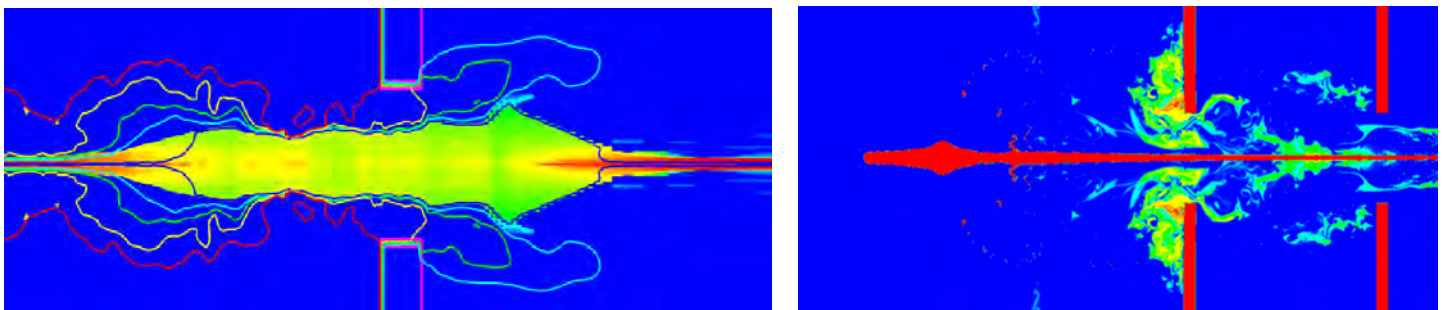

Figure 2: Electromagnetic armor: two example calculations of a shaped charge jet passing between two charged plates with holes. (left): plot of electric current streamlines and material densities for a high-current configuration. (right): plot of electrical conductivities for a low-current configuration.

Simulations are revealing new physics

For more information:
Technical Contact:
Erik Strack, Ph.D
505-284-9270
oestrac@sandia.gov

Science Matters Contact:
Alan Burns, Ph.D
505-844-9642
aburns@sandia.gov

American troops have been overwhelmed by the increasingly sophisticated threats used against their vehicles in the recent Middle Eastern wars. Current armor has not been enough to stop the American death toll from rising, and the heavily armored vehicles that can protect against these threats are so heavy that they cannot be airlifted nor drive over ordinary bridges.

The United States Army Research Laboratory (ARL) is addressing these issues by studying many exciting new armor technologies. One promising research area is electromagnetic armor, which can protect against some threats by subjecting the jet from a shaped charge explosive (Figure 1) to high electrical current flows and crushing electromagnetic forces

(Figure 2) that substantially decrease its penetrating capability. Some of the phenomena that occur in electromagnetic armor are so complex that ARL scientists have not been able to understand important trends in their experiments. To gain insight, ARL has chosen to enhance Sandia's ALEGRA shock and multiphysics simulation code [1] (originally developed to model experiments on Sandia's Z accelerator [2]) to build a near-first principles simulation capability for the complicated physics in electromagnetic armor. ARL scientists have been working closely with Sandia physicists and computational scientists over the last five years to develop advanced material models, improved numerical formulations of magneto-hydrodynamics, and efficient

Sandia National Laboratories

NNSA National Nuclear Security Administration
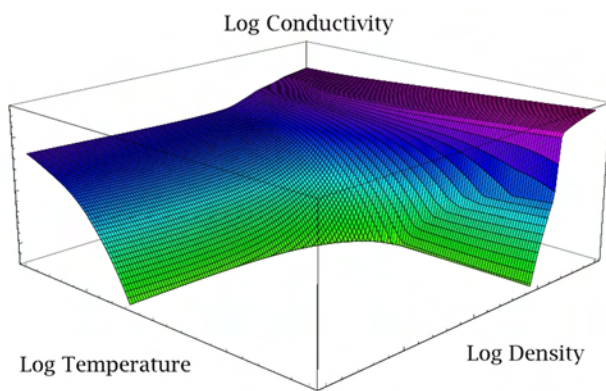
Figure 3: Illustration of an electrical conductivity surface. The conductivities in the original estimates of this surface were off by more than two orders of magnitude in the low-density, high temperature area of phase space.

solvers for massively parallel supercomputers to tackle this ambitious goal.

Scientists at both ARL and Sandia have been amazed by the tremendous differences made by new models for electrical conductivities of key materials. In the early stages of the project, the lack of accuracy in available models was identified as a crucial limiting factor in matching experimental results. For many materials, experimental data were simply not obtainable, and quantum-molecular dynamics simulations [3] were used to calculate conductivities in as-yet unexplored regions of phase space. In one instance, Sandia material scientists, motivated by ARL's experimental results, found differences of two orders of magnitude between existing estimates and their newly developed models (Figure 3).

Advanced numerical methods have also been crucial to the success of the project. Sandia determined that the numerical discretizations employed in the solution of Maxwell's equations must be compatible with the mathematical structure of these differential equations to preserve important characteristics of the magnetic field [4]. Furthermore, the linear solvers that use algebraic multigrid methods (necessary for these very large, difficult problems) required extensive reformulation [5] to obtain reasonable solution times on the thousands of processors required to solve the problems.

The ultimate goal of this work is to deliver a predictive simulation capability for electromagnetic armor. To meet this goal, Sandia is focusing considerable attention on verification of ALEGRA's computational methods. ARL, in turn, continues to run carefully calibrated experiments

that provide validation data for the models used. The project will continue to leverage new methods in material modeling and numerical algorithms to make the capability truly predictive.

The future for this work is bright: ARL analysts have been able to reproduce counter-intuitive electromagnetic armor experimental results [6], and the collaboration between the analysts and the experimentalists at ARL has become so strong that ALEGRA is now routinely used to predict experimental trends and important dynamic values (such as inductances) of components in experiments. The strong interaction between simulation and experiment has resulted in a valuable and fruitful partnership between the scientists at ARL and Sandia.

References:

1. Robinson, A.C., W.J. Rider (corresponding author), et al., "ALEGRA: An Arbitrary Lagrangian-Eulerian Multimaterial, Multiphysics Code," AIAA-2008-1235, Proc. 46th AIAA Aerospace Sciences Meeting, Reno, NV, January 2008. http://www.cs.sandia.gov/ALEGRA/Publications.html

2. Lemke, R.W., M.D. Knudson, A.C. Robinson, T.A. Haill, K.W. Struve, J.R. Asay, and T.A. Mehlhorn, "Self-consistent, two-dimensional, magnetohydrodynamic simulations of magnetically driven flyer plates," Physics of Plasmas, Vol. 10, No. 5, May 2003, pp. 1867-1874.

3. Desjarlais, M.P, J.D. Kress, and L.A. Collins, 'Electrical conductivity for warm, dense aluminum plasmas and liquids', Phys Rev E 66(2), p.025401/1-4, 2002.

4. Bochev, P.B. and A.C. Robinson, "Matching Algorithms with physics: exact sequences of finite element spaces", Collected Lectures on the Preservation of Stability under Discretization, edited by D. Estep and S. Tavener, chapter 8, SIAM, 2002.

5. Bochev, P.B., J.J. Hu, C.M. Siefert, and R.S. Tuminaro, "An Algebraic Multigrid Approach Based on a Compatible Gauge Reformulation of Maxwell's Equations," SIAM Journal on Scientific Computing, Submitted March 2007.

6. Doney, R.L., C.J. Garasi, and O.E. Strack, 'Modeling the Performance of Electromagnetic Armor with ALEGRA-MHD'. Proceedings of the Warheads and Ballistics Classified Symposium, Monterey, CA, February 11-14, 2008.

Computers and Information Sciences
Computational Simulations

Enabling Predictive Simulation through Embedded Sensitivity Analysis
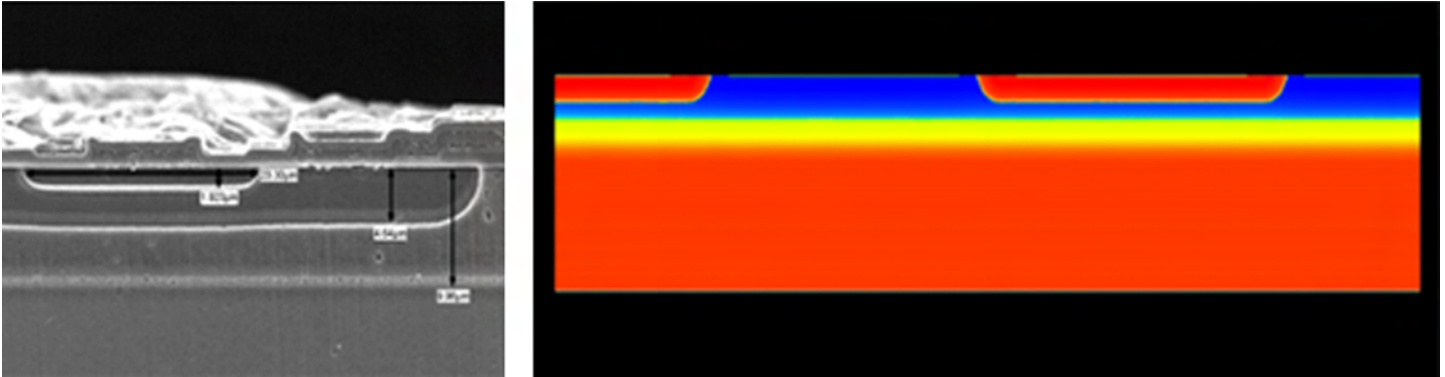

Figure 1: Left: Experimentally obtained micrograph of a stockpile bipolar junction transistor. Right: RAMSES/Charon simulation of the electric potential in the device.

Revolutionary approach uses automatic differentiation

For more information:
Technical Contacts:
Roger Pawlowski
505-284-3740
rppawlo@sandia.gov

Eric T. Phipps
505-284-9268
etphipp@sandia.gov

Science Matters Contact:
Alan Burns, Ph.D
505-844-9642
aburns@sandia.gov

Computational simulation plays a critical role in the design, risk assessment, and qualification of complex engineering systems relevant to Sandia's mission. Examples include the design of re-entry vehicles and stable fusion reactors, the licensing of nuclear reactors and waste repositories, and the qualification of electronics in radiation environments. *Predictive* simulation entails significantly more analysis than high fidelity simulations, rather, it additionally requires verification of simulation code correctness, validation of the simulation's effectiveness at modeling the system, measuring the sensitivity of simulation results with respect to input data, and quantifying the effects of uncertainty in this data. Accordingly, simulation and analysis tools must provide these capabilities with reasonable execution times for predictive simulation to be feasible.

Computing derivatives, a staple of any freshman calculus course, provides the foundation for many analysis algorithms supporting predictive simulation. Derivatives, also called sensitivities, determine how a computation's results vary with it's inputs, and are useful in (1) estimating how errors and uncertainties in those inputs affect simulation outcomes, (2) highlighting which physics or subsystems are most important in a simulation, and (3) calibrating simulations against empirical data. Thus, estimating derivatives quickly and accurately is critical for predictive simulation. Traditional sensitivity approaches for complex large-scale production codes are based on running repeated simulations while varying inputs. While this approach is simple and convenient, it disregards much of the knowledge of the underlying system that could be leveraged for more efficient computations. Recently, Sandia has developed revolutionary technologies for "embedded" sensitivity analysis based on the ideas of automatic differentiation. Where simulations normally compute solution values, this technology re-uses the same simulation code-base but automatically produces sensitivities along with the solution. This new capability allows researchers to extract very accurate sensitivity information from simulation codes using less computing time than traditional approaches, but with minimal impact on the software development cycle. By leveraging this capability, Sandia researchers can develop and apply significantly more accurate and
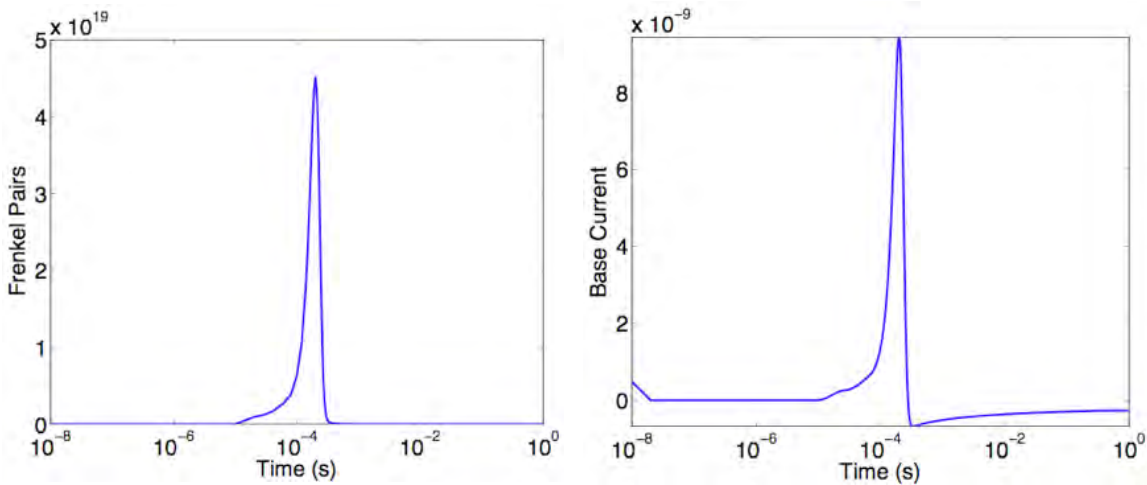
Figure 2: Left: Plot of the simulated radiation damage pulse, measured as the density of Frenkel pairs (defects in the device created by radiation) in the device from Figure 1, as a function of time. Right: Resulting electric current flowing through the base contact of the device as computed by RAMSES/Charon.

efficient derivative-based analysis algorithms to even the most complex science and engineering problems.

This technology has recently been showcased in the simulation of radiation damage of an electrical circuit (Figure 1) as part of the Qualification Alternatives to the Sandia Pulse Reactor (QASPR) project. Figures 1 and 2 show a stockpile bipolar junction transistor along with computational simulation of the device under radiation provided by the RAMSES/Charon (RAMSES=Radiation, Analysis, Modeling, and Simulation for Electrical Systems) simulation code. Using the embedded sensitivity technology, coupled with a state-of-the-art transient sensitivity analysis tool currently under development, Sandia researchers were able to determine which of the 126 parameters in the radiation damage mechanism the operation of the device was most sensitive to (Figure 3). This improved understanding of the damage mechanisms, and indicated where further modeling efforts are required to increase simulation fidelity. Furthermore, this technique was demonstrated to be approximately *14 times faster* than traditional techniques, and significantly more accurate and robust as well.

This pivotal work is rapidly being incorporated into Sandia's next generation simulation software. It has impacted a variety of internal projects including security and strategic evaluations of the national natural gas network, rail gun design, circuit network design, and fundamental magnetohydrodynamics research. Externally, this work has fostered a strong collaboration in modeling advanced tactical lasers for the U.S. Air Force as well as potential impact to oil and gas exploration.

The automatic differentiation capabilities are available in the Sacado software package, part of Sandia's open-source Trilinos Software Framework, located at http://trilinos.sandia.gov/. The transient sensitivity analysis capability is provided by the Rythmos package, also part of Trilinos.
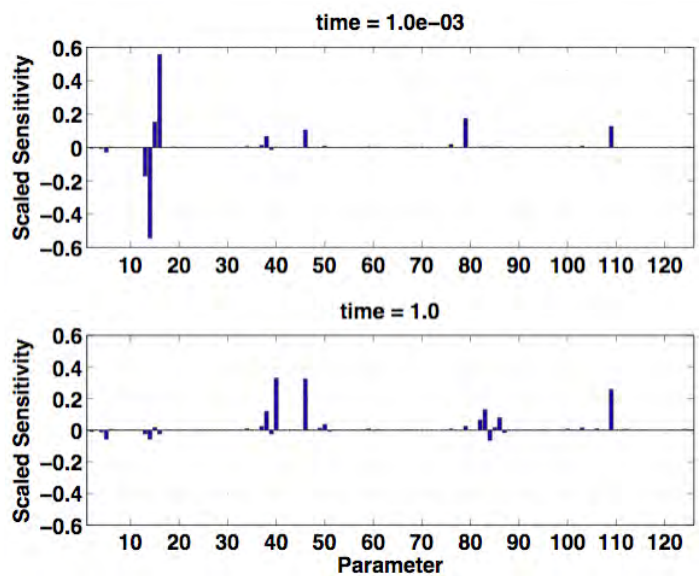

Figure 3: Plot of the scaled sensitivity of the base current from Figure 2 with respect to 126 parameters in the radiation damage mechanism, at early (top) and late (bottom) times after the radiation pulse. These results help focus future radiation damage mechanism research.
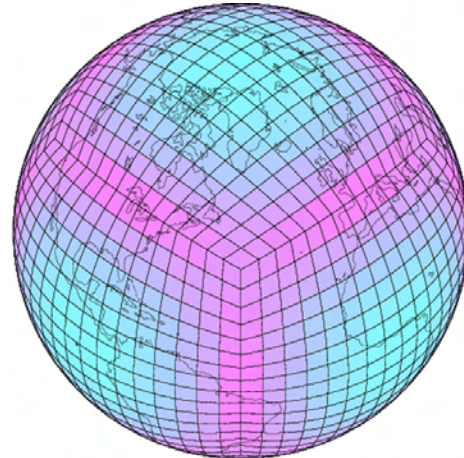
Computer and Information Sciences
Modeling and Simulation

Community Climate System Model Development for Petascale Supercomputers
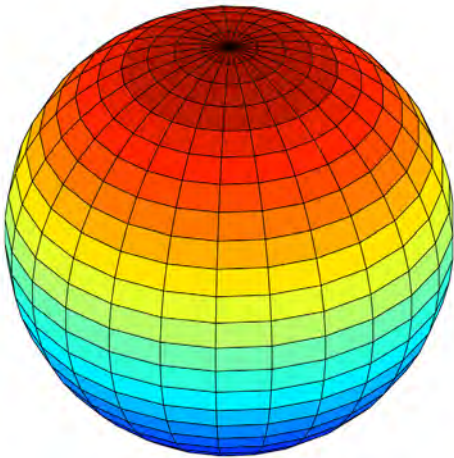
Figure 1: A latitude-longitude grid showing the clustering of grid points at the poles. This creates numerical difficulties in climate models which can be overcome, but at the cost of degrading parallel scalability.

Figure 2: The cubed-sphere grid used by the spectral element atmospheric model component of the CCSM. The color represents the area of each grid cell. The cells are much more uniform when compared to the cells in a latitude-longitude grid.

Predicting local impacts of climate change with next-generation computers

For more information:

Technical Contact:
Mark Taylor
505-284-1874
mataylo@sandia.gov

Science Matters Contact:
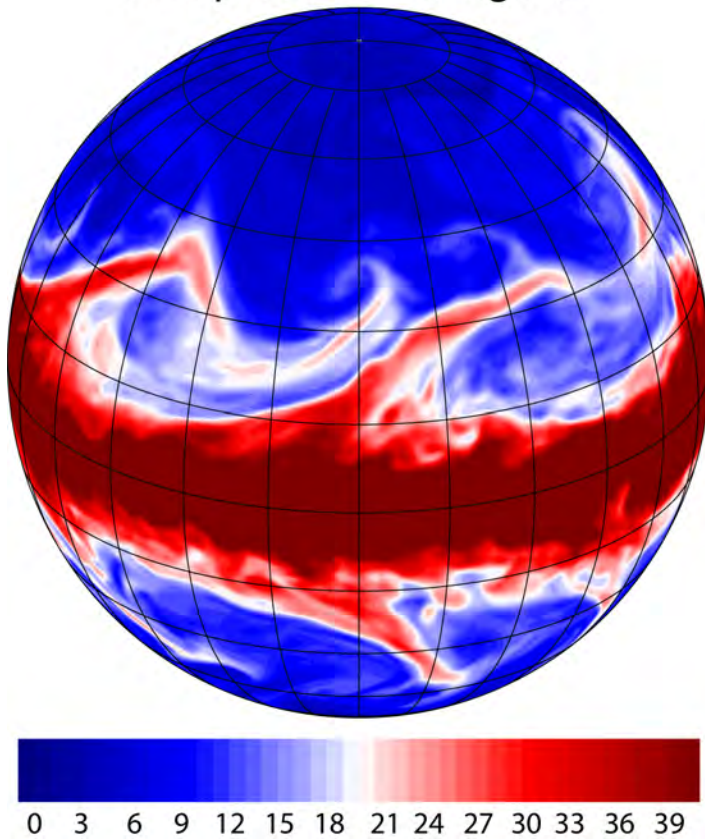Alan Burns, Ph.D
505-844-9642
aburns@sandia.gov

Climate change is already underway and will accelerate this century, but there are still major uncertainties. Human societies will respond with both mitigation and adaptation strategies, which may include changes in consumption of energy and other resources, land use, agriculture, and migration. These stresses could also lead to a shift in alliances and to civil unrest and conflict. Adapting to new situations will require advanced understanding of climate change and its direct and indirect effects. An improved understanding of climate change is of paramount importance for mission planning, surveillance, facilities placement and design, and sustainable energy futures. Developing this understanding requires high fidelity climate models which simulate many components of the Earth system, including atmospheric and oceanic circulation, land surface processes, sea ice, and chemical and biogeochemical cycles. Adding full chemical and biogeochemical cycles to today's climate models will require significantly more computational resources than available today. Furthermore, an increase in resolution to allow for the accurate assessment of regional impacts of climate change also requires further increases in computational power. Achieving both of these goals will require petascale computer architectures.

The Department of Energy's (DOE) upcoming petascale computers will have hundreds of thousands of processors. Effectively using such machines remains a challenge due to several scalability bottlenecks present in all modern climate models, the largest of which is created by the numerical methods used in the *dynamical core* of the atmospheric model component. The dynamical core solves the partial differential equations governing the fluid dynamical aspects of the atmosphere. In addition, atmospheric models contain a suite of subgrid parametrizations for the many physical processes unresolved in an atmospheric model but which drive the dynamics such as convection, precipitation

Sandia National Laboratories

National Nuclear Security Administration

Precipitable water kg/m2

0 3 6 9 12 15 18 21 24 27 30 33 36 39

Figure 3: A snapshot of precipitable water over the surface of an Aqua planet, simulated using the atmospheric component of the CCSM with the spectral element dynamical core on a cubed-sphere grid. Aqua planet simulations are used to test new dynamical cores and other physical processes in climate models before coupling with other components such as land, ocean and ice models. The color scheme is suggestive of clouds, but we note that even on petascale computers, climate models will lack sufficient resolution to directly model clouds. Instead, the effects of clouds on the resolved scales are modeled with subgrid parametrizations.

and radiative forcings. Currently, most dynamical cores use latitude-longitude based grids (Fig. 1). These grids create a logically Cartesian orthogonal mesh suitable for a wide array of numerical methods, including finite volumes and the spectral transform method. The grid lines cluster at the pole, creating several computational difficulties collectively referred to as the *pole problem*. One such difficulty comes from the Courant-Friedrichs-Lewy restriction, which tells us that this clustering requires the dynamical core to compute many more timesteps than would otherwise be necessary. This would result in a simulation that should take days to complete now requiring a few months instead. There are many successful techniques to handle this pole problem, however most of them substantially degrade parallel scalability by requiring too much inter-processor communication.

Team members at Sandia, the National Center for Atmospheric Research, and Oak Ridge National Laboratory, all lead by Mark Taylor, have thus been focusing on the development of new, more scalable dynamical cores based on cubed-sphere grids (Fig. 2) for the Community Climate

System Model (CCSM), the U.S. flagship climate change model. They have recently developed a new formulation of the highly scalable spectral element dynamical core tailored to the needs of the CCSM. This work has lead to unprecedented scalability in the atmospheric component. It can now run efficiently on 86,000 processors when using a horizontal average grid spacing of 25 km. Even better scalability will be possible when computing with a global resolution of 10 km, DOE's long term goal. The team has completed extensive verification work using standardized atmospheric tests with prescribed surface temperatures but without the CCSM land, ice or ocean models (Fig 3). The team is currently focused on coupling with these other CCSM component models.

Energy and Resources
Solar Energy

Sunshine to Petrol
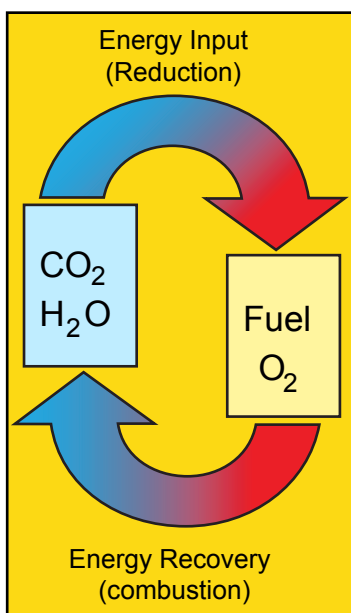
Figure 1: The S2P process incorporates CO_2 into the vision for the Hydrogen Economy powered by the sun.

High efficiency thermochemical heat engine for production of synthetic fuels
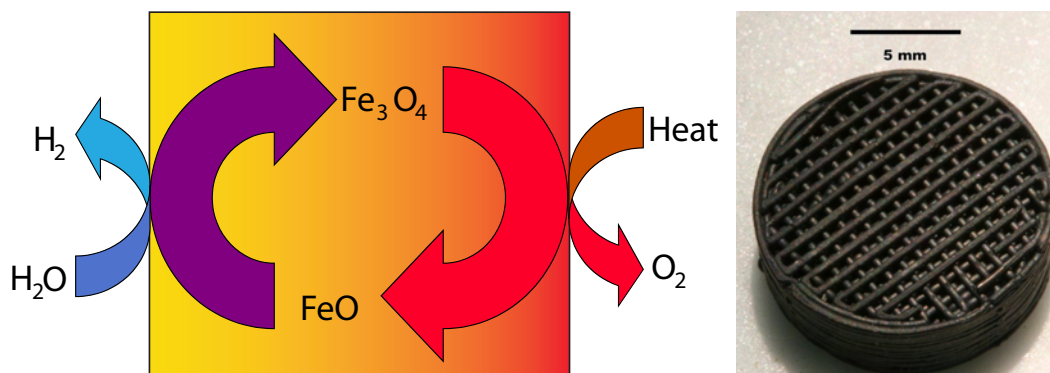
For more information:
Technical Contacts:
James E. Miller
505-272-7626
jemille@sandia.gov

Nathan P. Siegel
505-284-2033
npsiege@sandia.gov

Science Matters Contact:
Alan Burns, Ph.D
505-844-9642
aburns@sandia.gov

Figure 2: Left: The iron oxide or ferrite cycle is the archetype of metal-oxide thermochemical cycles. The CR5 prototype employs mixed-metal cobalt ferrites supported in a zirconia matrix. In one chamber concentrated solar irradiation heats the ferrite to high temperature driving off oxygen. In the opposite chamber the oxygen deficient ferrite is exposed to CO_2 or H_2O at a lower temperature to produce CO or H_2. Heat is recuperated between the two reaction chambers by driving neighboring reactive rings countercurrent to one another. Right: Monolithic laboratory test sample fabricated directly from a cobalt ferrite/YSZ composite. Lattice structure provides high geometric surface area area. (Scale bar = 5mm)

Solar irradiation is the only sustainable energy source of a magnitude sufficient to meet projections for global energy demand. Solar fuels (i.e., fuels created from sunlight, carbon dioxide, and water) are especially attractive as they impact not only energy production and climate change, but also energy storage and energy security. Applying a solar energy source to chemically "reverse combustion" and produce liquid hydrocarbon fuels that are compatible with our current infrastructure from CO_2 and H_2O (Figure 1) is an extension of the hydrogen economy that is analogous to the process of photosynthesis. However, by directly applying concentrating solar power to the problem of splitting CO_2 and H_2O to produce CO and H_2, the basic energy-rich building blocks of synthetic liquid fuels, Sandia researchers are optimistic that sunlight-to-fuel efficiencies will be significantly improved. The researchers call this unique approach of re-imagining the transportation fuel paradigm "Sunshine to Petrol" or S2P.

The heart of the S2P process is a unique metal-oxide-based thermochemical heat engine, the Counter-Rotating-Ring Receiver Reactor Recuperator, or CR5. Within the engine, rings of a reactive solid are thermally and chemically cycled to produce O_2 and CO or H_2 from CO_2 or H_2O in separate and isolated steps (Figure 2). These steps require high temperatures (ca. 1500 °C) that are achieved by concentrating solar power. The CR5 is a thermochemical analog to Stirling and Ericsson cycle heat engines and provides a framework for maximizing efficiency. Thus a key feature of the CR5 is the counter-current recuperation of heat between the high temperature O_2-generating thermal reduction of the metal oxide and the lower temperature H_2- or CO-producing oxidation of the metal oxide that improves the overall efficiency of the thermochemical process.

This CR5 is very demanding from a materials point of view. The active rings must maintain structural integrity and high reactivity after extensive thermal cycling.
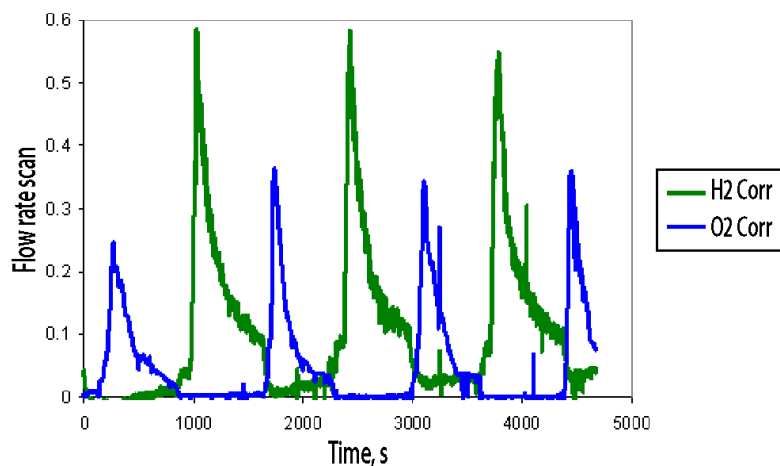
Figure 3: Hydrogen and oxygen are produced over successive cycles in a 2:1 ratio in a solar furnace evaluation of a cobalt ferrite/YSZ monolith (thermal reduction at 1580 °C, water oxidation at 1050 °C).
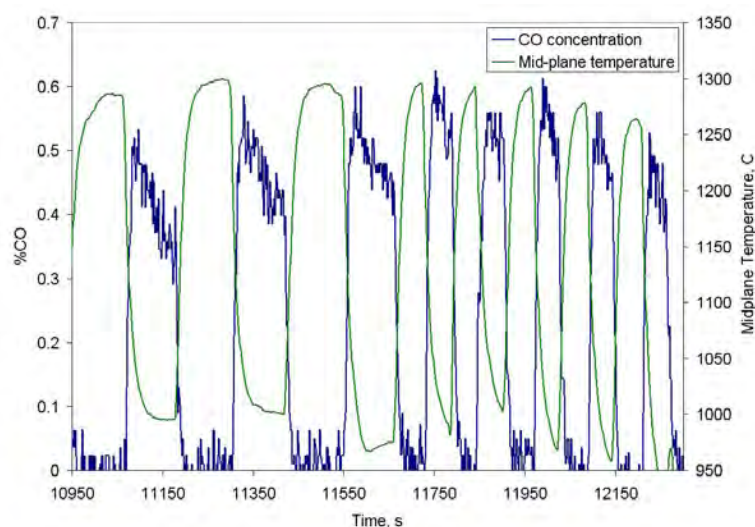

Figure 4: CO produced over a cobalt ferrite/YSZ monolith in a solar furnace evaluation. The data demonstrates that reduction times as brief as one minute are sufficient to yield CO when the monolith is subsequently contacted with CO_2.

In addition, the monolithic ring structures must have high geometric surface area for gas-solid contact and for adsorption of incident solar radiation. It was found that directly fabricating structures from the active components of cobalt ferrite and yttria-stabilized zirconia yields robust and active monolithic parts (Figure 2) that maintain productivity over tens of cycles of laboratory and solar testing (Figure 3). Furthermore, it has been demonstrated for the first time that CO_2 splitting to CO and O_2 can be conducted with both iron- and cerium-based materials in a cyclic manner (Figure 4). Testing of the CR5 prototype containing over 5kg of active materials will commence during the summer of 2008.

Reference:

James E. Miller, Mark D. Allendorf, Richard B. Diver, Lindsey R. Evans, Nathan P. Siegel, and John N. Stuecker "Metal Oxide Composites and Structures for Ultra-High Temperature Solar Thermochemical Cycles" J. Mater. Sci. (2008) 43:4714–4728.

Engineering Sciences
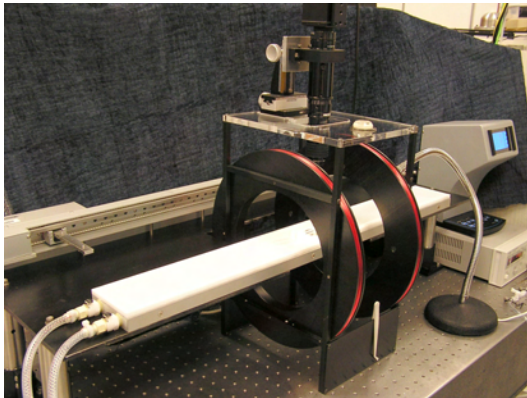## Fluid Processes

Physics of Liquid Interfaces

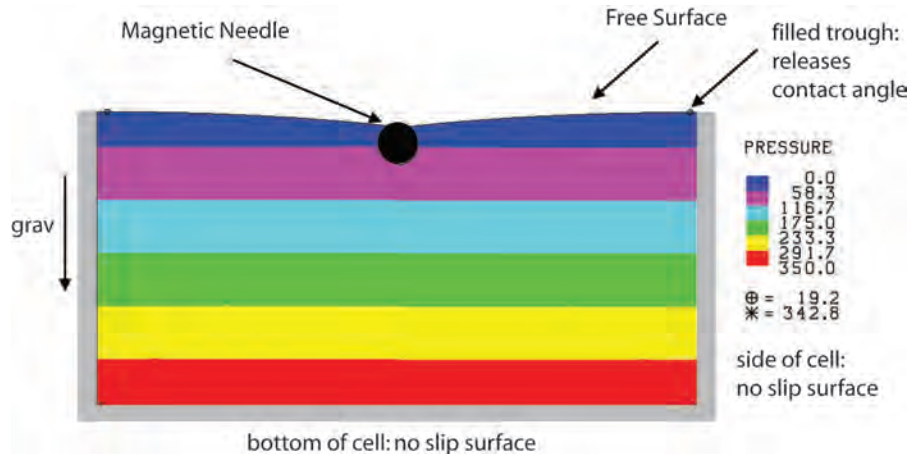**Figure 1:** Interfacial stress rheometer (ISR)

Figure 2: Finite element model of the floating needle in the ISR. Fluid is allowed to determine its own location based on the surface tension, contact angle, and weight of the needle, resulting in the slightly curved shape of the interface.

Sandia leads in both interfacial measurements and modeling

For more information:
**Technical Contact:**
Lisa Mondy
505-844-1755
lamondy@sandia.gov

Science Matters Contact:
Alan Burns, Ph.D
505-844-9642
aburns@sandia.gov

Flow of liquid through a pipe or air past a fin involves processes dominated by viscosity or inertia. However, as applications shrink to microscopic sizes there is a huge increase in the ratio of surface area to volume, and other phenomena such as surface tension, surface viscosity, and diffusion can begin to predominate. In addition to microfluidics, many macroscopic applications with large surface areas, such as foams and emulsions, have properties that are strongly influenced by interfacial phenomena. Interfacial properties are distinct from bulk properties on either side of the boundary, are not well understood, and are difficult to predict. Furthermore, although one can almost always assume that a bulk liquid under ordinary conditions is incompressible, an interface can stretch, and the dilatational terms in the momentum equation can no longer be ignored.

Sandia is at the cutting edge of both fluid interfacial property measurements and modeling. The interfacial stress rheometer (ISR, Fig. 1) uses a Langmuir trough to prepare monolayers of insoluble surfactant with a desired surface density at an air-liquid interface [1]. A Teflon-coated magnetized needle is freely suspended at the interface due to surface tension forces. A periodic magnetic field is applied to the needle, and, from the amplitude and phase shift of the periodic needle displacement, the viscoelastic properties of the interface are measured. Since the needle's response is affected by both the interface and the underlying liquid subphase, a key issue is to separate out the bulk rheological response of the system from the surface rheological response; this is done via a numerical model. The curvature of the interface can be determined through finite element modeling (Fig. 2).

A surface dilatational rheometer (SDR, Fig. 3) is used to measure the mechanical resistance to surface deformations resulting from changes in surface area [2]. Similar to a pendant drop tensiometer, where surface tension is measured by fitting the shape of a hanging drop to a solution to the Laplace equation of capillarity, the SDR uses the pendant drop technique to measure changes in surface
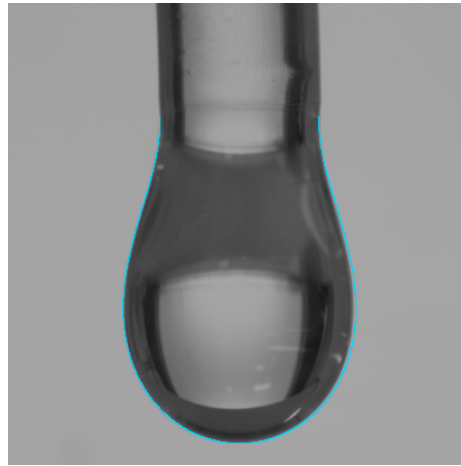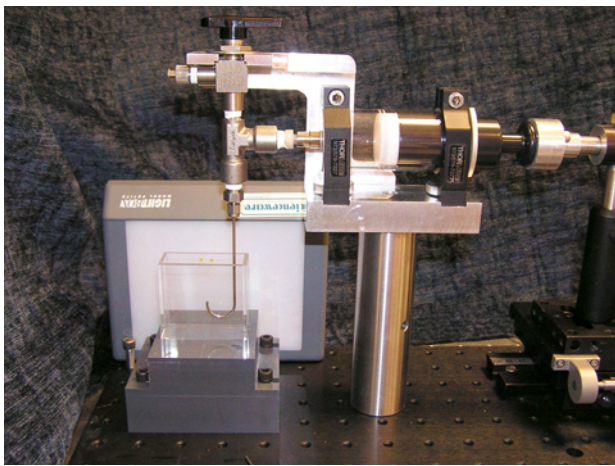
Figure 3: Left: Surface Dilatational Rheometer (SDR). Right: related pendant drop imaging used to determine surface tension.
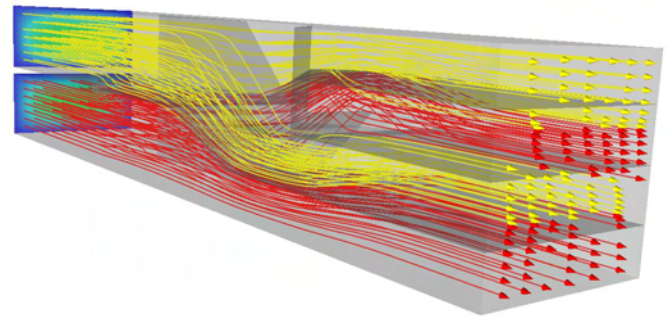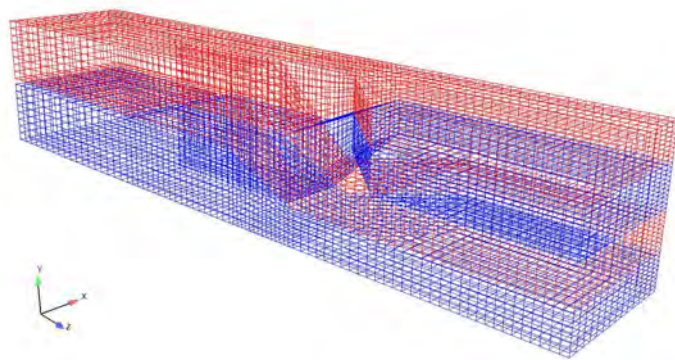
Figure 4: Finite element mesh (left) and calculated particle paths (right) of a coextruder where two initial layers are multiplied to four.

tension of an oscillating droplet. A time-dependent surface area is generated by varying the drop volume, and the resulting changes in surface tension are analyzed to measure an effective surface dilatational modulus.

Experimental discovery is key to the ongoing development of surface rheological models included in Sandia's engineering codes. Hence, it is also the key to the ability to describe the physical behavior of systems in advanced manufacturing techniques -- processes such as creating polymer membranes by reaction at a liquid interface in a microfluidic device [3] or coextrusion to form a composite of fine polymer layers [4] (Fig. 4). In addition, interfacial physics controls the stability of a foam or emulsion and, therefore, impacts the formulation and production of a wide variety of consumer products from whipped cream to pharmaceuticals. It also impacts the optimization of electronic encapsulation processes for our nuclear weapons and de-foaming strategies for eliminating particle-stabilized foams in processing nuclear wastes.

References:

1. S. Reynaert, C.F. Brooks, P. Moldenaers, J. Vermant, G.G. Fuller, *Journal of Rheology* **52**, 261-285 (2008).

2. E. M. Freer, T. Svitova, and C. J. Radke, *J. Petroleum Sci. Eng*. **39**, 137-158 (2003).

3. J. Atencia and D. Beebe, *Nature* **437**, 648-654 (2005).

4. R. R. Rao, R. Collins, R. Mrozek, J. Lenhart, R. Schunk, M. Hopkins, P. Notz, and L. Mondy, "Finite Element Analysis of Multilayer Coextrusion," Proceedings of the 24th Meeting of the Polymer Processing Society, Salerno, Italy, June 15-19, 2008.

Engineering Sciences
Radiation Effects

Photonic Displacement Interferometer for Material Measurements in Extreme Environments

Figure 1: Basic elements of the PDI system. The circulator is a three port miniature photonic device that performs the function of a laser beam splitter. The focusing lens probe interrogates the specimen surface, and the circulator directs the retroreflected light to the 3x3 coupler. The reference leg provides the unshifted laser light that interferes with that returned from the probe leg as the two signals are mixed in the 3x3 coupler. The output of the 3x3 coupler consists of three optical signals which are 120 degrees out of phase with each other. The relative phases of these three signals give the direction of the surface motion. (see Fig. 2).

Versatile instrument provides direction-sensitive information for fast material response studies

For more information:
Technical Contact:
Scott C. Jones, Ph.D
505-284-0165
scjones@sandia.gov

Science Matters Contact:
Alan Burns, Ph.D
505-844-9642
aburns@sandia.gov
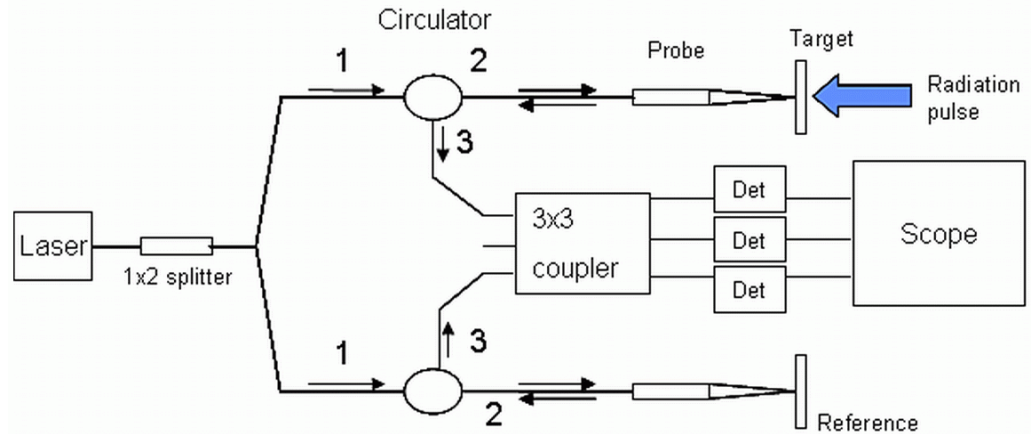
Laser interferometry is a natural choice for dynamic material response measurements, especially in environments high in EM (electro-magnetic) noise, such as Sandia's pulsed power accelerators. In the 1960s and 1970s, the bandwidths of electro-optic transducers and oscilloscopes limited the usefulness of displacement interferometry to material velocities less than 100 m/s. The development of the VISAR (Velocity Interferometer System for Any Reflector) at Sandia in 1972 [1] provided a solution to these limitations, and has been a work horse for material response measurements ever since. VISAR, however, has its own set of constraints on interpreting material response data, especially for what may now be termed 'low speed' measurements, and when measuring complex material or structural responses to flyer impacts or radiation pulses. The evolution of technology is such that instrument bandwidths have improved about 100-fold since then, and a concurrent development of photonic technology has led to a re-examination of displacement interferometry for basic measurements of material response in extreme environments.

Lawrence Livermore National Lab [2] developed the first Photonic Doppler Velocimeter system based on a fiber laser, a fiber optic circulator, a simple lensed probe, a fast detector and an oscilloscope, resulting in a velocimetry system that has essentially one single adjustment. However, the data can be difficult to interpret in terms of surface displacement where complex motions are involved, and are generally reduced using Fourier techniques to extract surface velocity. Sandia has solved these problems by incorporating an easy-to-use, all fiber-optic displacement interferometry system with a directionally-sensitive data reduction routine [3], tailored to the needs of measuring material and structural response to intense radiation pulses (Fig. 1). Since data is analyzed in terms of displacement, the system is called the Photonic Displacement Interferometer (PDI).

As shown in Fig.1, the reference leg of the PDI provides the unshifted laser light that interferes with that returned from the probe leg as the two signals are mixed in the 3x3 coupler. The output of the coupler consists of three optical signals which are 120 degrees out of phase with each other. The relative phases of these signals are what allow automated data reduction to occur – whether the phase of one signal 'leads' or 'lags' the others depends on the direction of the surface motion (Fig. 2).
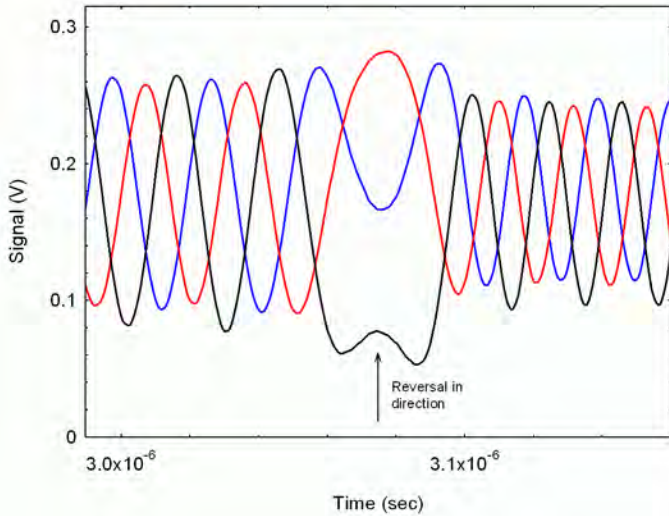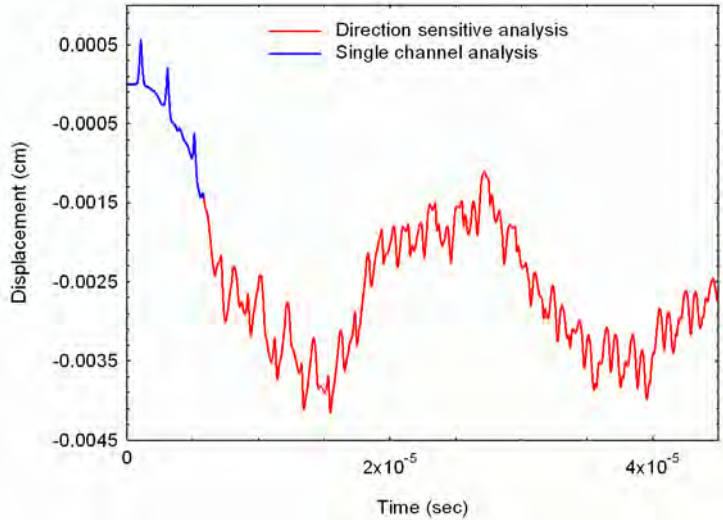
Figure 2: The three interference 'fringe' signals obtained from PDI system. Note the fringe order for times before the reversal – red, black, blue – changes after the reversal. This allows automated data analysis. If only the red signal were recorded, the reversal would be difficult to identify.


Figure 3: Time resolved displacement of simple aluminum disk irradiated by an high intensity electron beam pulse.

Two of the greatest advantages of this system are the noncontact nature of the measurement (the measurement does not perturb the response), and the immunity to EM interference. Thus material response measurements in the extreme EM environments of Sandia's Saturn and Z pulsed power facilities have been obtained without measurable disturbance of the optical signals.

As an example, Figure 3 shows the response of a simple aluminum disk to an high intensity, 10 nsec pulse of electrons. The detailed motion is complex, showing response to thermomechanical shock superposed with the structural response of the disk. The details have subnanosecond time resolution. Without the direction sensitive analysis capability, the motion cannot be reliably interpreted beyond about 5 microseconds.

A recent collaboration with the Atomic Weapons Establishment in England focused on time-resolved measurement of the impulse resulting from x-ray induced material blow off. In these experiments, a thin film of low vaporization enthalpy metal (Au/Bi) is applied to a substrate. The momentum imparted to the sample is determined by the average velocity, and details of the process are given by the subnanosecond resolved detail (Fig. 4).

The present system can measure three points on a sample. A 2 Watt laser provides enough light to interrogate up to 20 sample points. A number of these systems are currently being assembled at Sandia for applications beyond radiation response testing, including gas gun and isentropic compression testing, and various diagnostic applications at the Z accelerator. Demonstration as an impulse diagnostic for Sandia's Light Initiated High-Explosive Impulse Facility is planned for the fall.
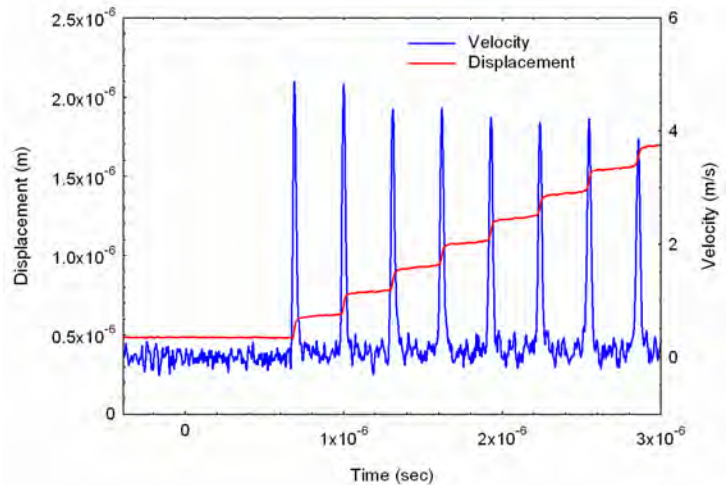
Figure 4: Response of a thin gold foil to an x-ray pulse from an Argon gas puff Z pinch in SNL's Saturn accelerator. The gross impulse imparted to the sample via blow off can be determined by the average slope of the displacement data. The spikes in the velocity curve represent the thermomechanical shock response of the foil.

References:

1. L.M. Barker and R.E. Hollenbeck, J. Appl. Phys. **43**, 4669 (1972).

2. O.T. Strand, D.R. Goosman, C. Martinez, T.L. Whitworth and W.W. Kuhlow, Rev. Sci. Instrum. **77**, 083108 (2006).

3. D.H. Dolan and Scott C. Jones, Sandia Report SAND2008-3871 (2008).

Engineering Sciences
Thermal Science

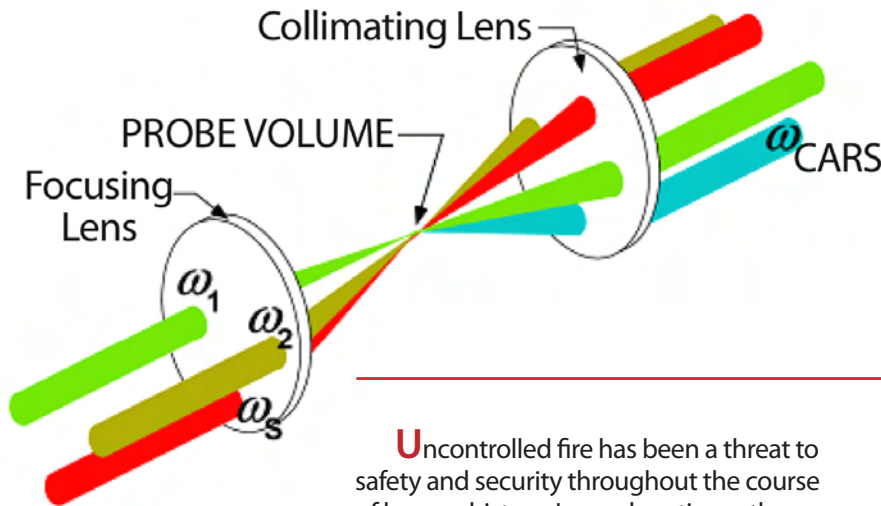# Laser Diagnostics Reveal the Nature of Fire

Figure 1: Arrangement of laser beams for a CARS measurement.

Temperature, composition and flow structure of fires

For more information:

Technical Contacts:
Sean P. Kearney, Ph.D
505-844-6669
spkearn@sandia.gov

Timothy J. O'Hern, Ph.D.
505-844-9061
tjohern@sandia.gov

Science Matters Contact:
Alan Burns, Ph.D
505-844-9642
aburns@sandia.gov

Uncontrolled fire has been a threat to safety and security throughout the course of human history. In modern times, the danger posed by a fire accident is a dominant threat to our nation's infrastructure and to the security of our weapon systems. At Sandia's Thermal Test Complex, scientists and engineers are utilizing the power of high-energy pulsed laser light to provide new insight into the nature of fire, with measurement times on the order of light speed, and measurement volumes comparable to the size of a human hair— extreme resolution which is needed to resolve the physics of the fundamental flame zones which are the "building blocks" of even the largest fires.

Coherent anti-Stokes Raman scattering (CARS) is a spectroscopic tool which provides simultaneous temperature and gas-concentration data by probing the energy contained in the vibrations and rotations of gas molecules in a fire. With CARS, three selected laser wavelengths, shown in red, green and yellow in Fig. 1, are mixed in a nonlinear fashion, resulting in the generation of a blue-shifted CARS signal beam in the measurement volume. The spectral content of the CARS beam reveals the presence of combustion gases as distinct peaks in the CARS spectrum, as shown in Fig. 2; the fire temperature and gas composition can be obtained from the shape and relative strengths of these peaks. For example, recent
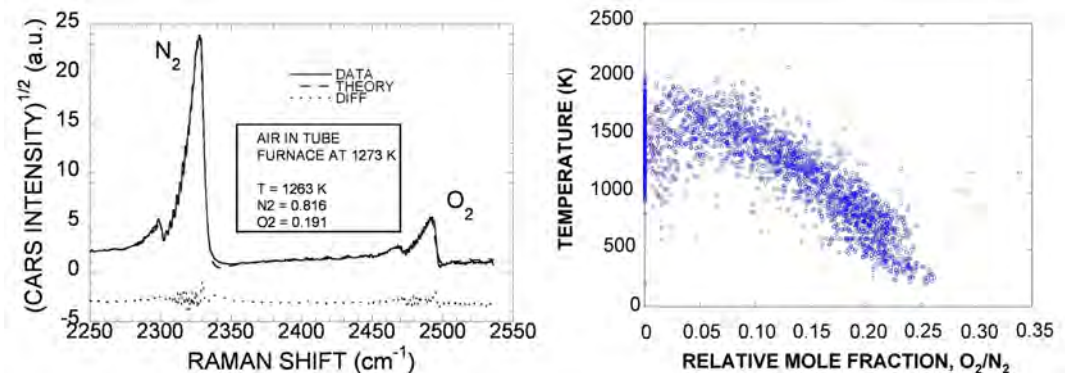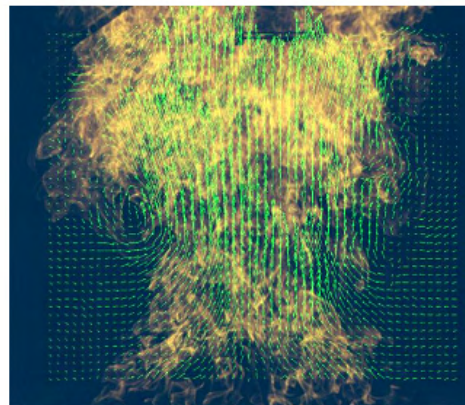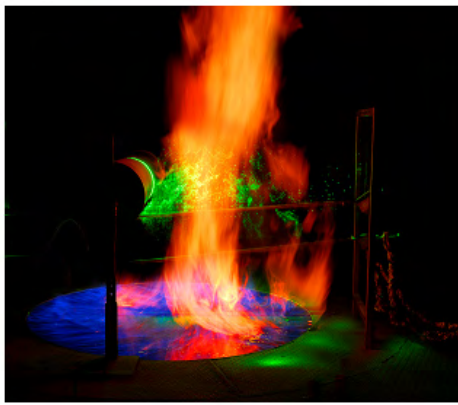

Figure 2: Left: CARS spectrum showing contributions from nitrogen and oxygen. Right: Temperature-oxygen correlation from a methanol fire.

Sandia National Laboratories

NNSA National Nuclear Security Administration

Figure 3: Left: PIV in a methanol fire. Green light from an Nd:YAG laser sheet can be seen scattering from PIV seed particles. Right: PIV-measured velocity field overlaid on visible image of soot emission from a methane fire.

experiments in a 2-m-diameter methanol pool fire revealed the correlation between temperature and oxygen content at a point in the middle of the pool (Fig. 2).

In order to reveal the nature of the complex turbulent flow field within a fire plume, Particle Image Velocimetry (PIV) is used. PIV provides a snapshot of the flow structure by tracking small, micron-scale particles which are introduced or "seeded" into the fire and follow the motion of the fire gases. The particles are illuminated for extremely short exposures to effectively "freeze" the particle motion using a 10-nanosecond laser light pulse that is formed into a two-dimensional light sheet. Laser illumination of particles in a 2-meter methanol fire is shown in Fig. 3. A picture of the velocity field is obtained by statistically correlating two successive freeze-frame particle images to track the particle motion between frames. A sample velocity field from a 1-m-diameter methane fire is also provided in Fig. 3, where the direction of gas motion is shown by green arrows whose length is proportional to the speed of the motion.

The high-fidelity experimental detail offered by these laser-diagnostic approaches is providing results which are used to validate the performance of advanced fire simulation tools being developed at Sandia. These state-of-the-art computer codes are used to perform high-consequence risk analysis for DOE weapon systems, military hardware and US critical infrastructure.

Robotic Direct Write Materials
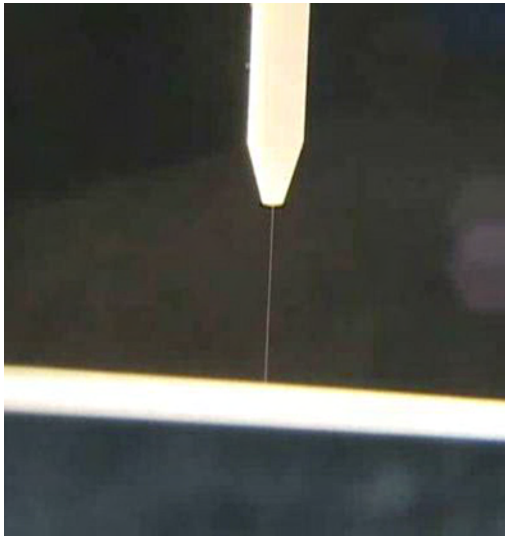
Figure 1: Ink jet of silver nanoparticles printed onto a circuit board. The print jet is only 30μm across.

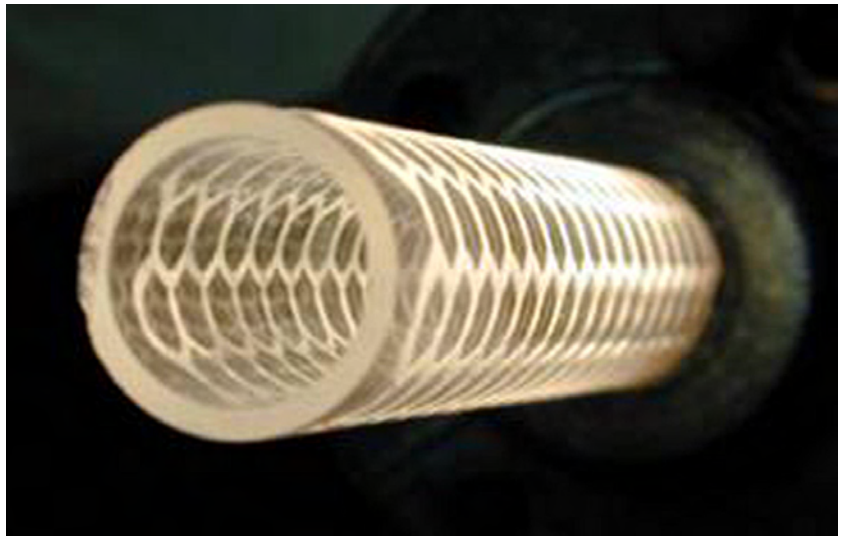**Figure 2:** 3D complex shape direct-printed onto a curved substrate. Conductors in this shape become highly sensitive antennas.

Augmenting COTS devices by post processing

For more information:
Technical Contacts:
Paul Clem
505-272-7624
pgclem@sandia.gov

Chris Apblett
505-272-7125
caapble@sandia.gov

Science Matters Contact:
Alan Burns, Ph.D
505-844-9642
aburns@sandia.gov

Today's requirements for new weapons and surety components require an ever-increasing accuracy of fabrication and amount of integration to allow for compact devices with more sophisticated capabilities. At the same time, cost and budget drivers provide an incentive for the use of commercial "off-the-shelf" devices (COTS) to be used. It is rare, however, that these COTS devices provide the full range of capability that is desired, or come in the form factor appropriate for a specific application. Thus, what is often needed is a low cost and versatile back-end capability to modify the functionality of COTS-type parts with a wide range of materials to enable further integration. It is this technology gap that Sandia's Direct Write capability aims to fill.

Direct Write technology utilizes a robotically-controlled printing tip (Fig. 1) to accurately deposit controlled amounts of nanoparticle-based slurries onto a substrate. Depending on the composition of the slurry, the deposited material is subsequently annealed to develop a densified microstructure with appropriate electronic, dielectric, catalytic, or optical properties. By choosing the starting nanoparticle size and composition, a wide variety of materials can be printed, from catalysts to quantum dots to electronic conductors with electrical properties close to that of the bulk. Additionally, control of the rheology of the slurries allows some of these materials to be cast either conformally on a 3D surface or across an unsupported span, allowing the fabrication of 3D lattices with complex geometries that cannot be fabricated using conventional machining techniques (Fig. 2).

The heart of Sandia's capability in direct write lies in combining both mechanical engineering (robotic printing from computer aided design, or CAD, files) and fundamental materials science (development of printable inks for

Sandia National Laboratories

LDRD
LABORATORY DIRECTED RESEARCH & DEVELOPMENT

Figure 3: A COTS radio frequency ID tag embedded in 100 μm wide silver antenna lines directly written on a flexible substrate. Mating a tuned antenna to this COTS chip enhanced the range of activation of the chip significantly.
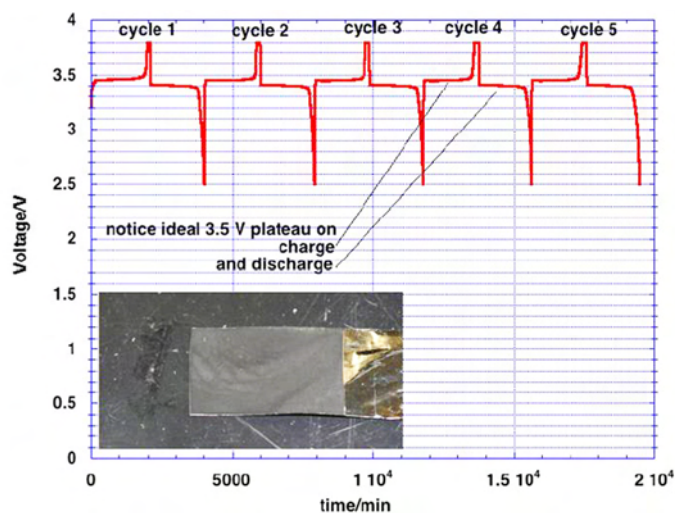
Figure 4: Performance of LiFePO$_4$-printed thin film cathodes in a test battery configuration, showing good charge/discharge characteristics, despite being very thin and flexible. Each charge cycle (increasing voltage with time) moves lithium out of the iron phosphate, and each discharge cycle (decreasing voltage with time) moves lithium back into the iron phosphate. A flat discharge profile (unchanging voltage vs. time) is indicative of good battery performance.

functional devices). By controlling the rheology of the slurries, materials precursors containing nanoparticles can be made as fluid as water or as thick as clay, allowing a wide range of shapes to be created. In contrast, traditional inkjet printing can print only a narrow range of viscosity in a planar array. Once a direct write slurry chemistry is defined, the robotic system uses a 2D or 3D CAD file to accurately control the deposition of the material. As an example, an ink composed of silver nanoparticles using a xylene-based solution can be printed conformally onto a surface with dimensions below 100μm to define a printed antenna or other conductive trace (Fig. 3). The resultant silver lines or patterns are annealed at 120ºC to produce a dense, conductive line suitable for connecting electronic circuits on a flexible substrate, or for making radio frequency antennas printed on curved surfaces. Alternatively, a paste composed of lithium iron phosphate, a cathode material for lithium ion batteries, can be cast into a highly porous structure, allowing for a high surface area of the cathode and subsequent increased rate capability of the battery (Fig. 4).

A fundamental understanding of nanoparticle sintering mechanisms is also critical, because this affects the final microstructure and properties of the printed material. Energy can be applied to printed slurries in various ways, either by traditional thermal annealing of the sample, by laser annealing, or even use of intense flashes of high energy photons to rapidly sinter the material. The effects of precursor particle morphologies, means of introducing energy for sintering, and understanding the interplay between processing and properties are areas of current research. As new nanomaterials are synthesized, they become the basis for a novel printed device capability; current examples of such nanomaterials are germanium nanoparticles and carbon nanotubes for printing semiconductor inks, biocompatible "bone scaffolding" ceramics, and polymer precursors for new coatings and subcomponent hermetic seals. From these applications, new fundamental science surrounding the densification of these materials is generated, leading to further understanding of nanoparticles and the effects of nanostructure and microstructure on functional properties

Materials Science and Technology
Nanocomposites

Rheology of Nanoparticle Suspensions

Diversity of nanoparticle interactions requires modeling at multiple length scales
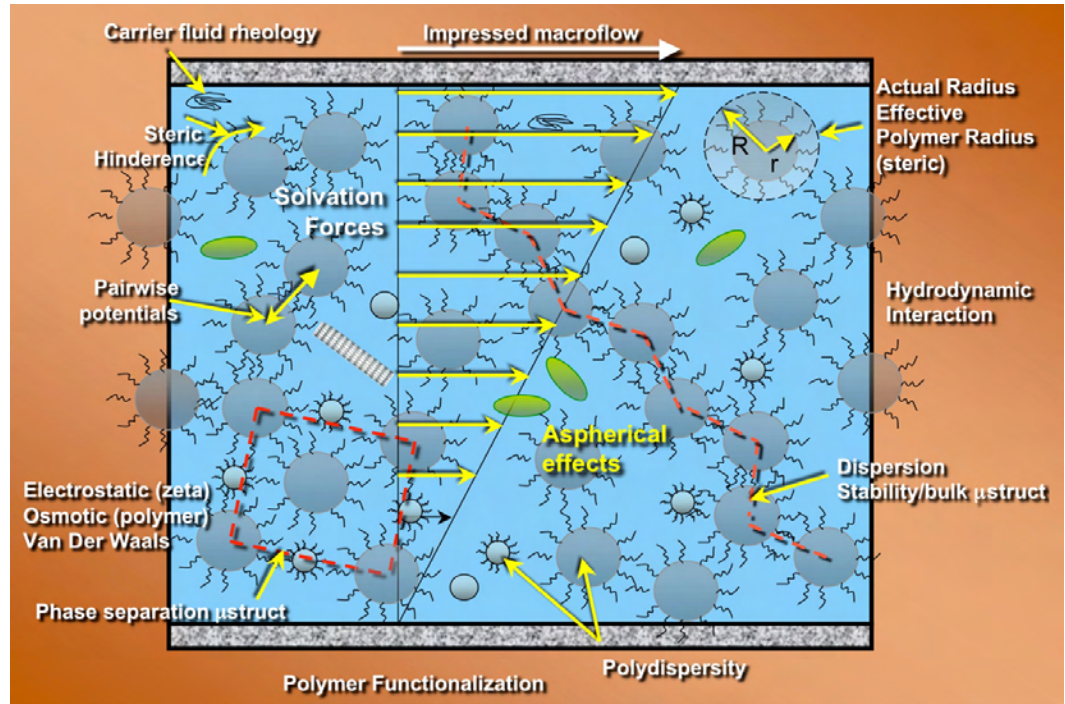
Figure 1: Illustration of the rich physical phenomena that control nanoparticle stability and rheology.

For more information:
Technical Contacts:
Gary S. Grest
Jeremy B. Lechman

P. Randall Schunk
505-844-3261
gsgrest@sandia.gov

Science Matters Contact:
Alan Burns, Ph.D
505-844-9642
aburns@sandia.gov

The growth of advanced nanoparticle fabrication techniques and analytical instrumentation has renewed the colloidal chemistry field and its application to nanoparticle composite manufacturing. Due to their small size, ranging from one to hundreds of nanometers, nanoparticles are mass efficient for modifying bulk and surface properties. They can now be made from a wide range of materials with unprecedented control of size and shape. There is also a rich set of possible nanoparticle coatings, particularly using the biochemistry of peptides and DNA, yielding new surface interactions. A distinct advantage of nanoparticles is that highly efficient and inexpensive polymer processing methods can be used to fabricate significant quantities of the composite material. Composites consisting of dispersed or ordered nanoparticle building blocks can be tailored to exhibit materials properties that have been unachievable with conventional materials,

including increased strength and toughness of films and fibers to enhanced optical characteristics of coatings.

The most feasible way to disperse particles in a bulk material or control their packing at a substrate is through fluidization in a carrier that can be processed with well-known techniques such as spin, drip and spray coating, fiber drawing, or casting, followed by solidification via solvent evaporation, drying, curing, and sintering. Unfortunately, processing nanoparticles as concentrated, fluidized suspensions is a primary challenge and remains an art largely because of the extraordinary effect of particle shape and volume fraction on fluidic (rheological) properties. A second challenge is to create stable dispersions that can be processed into films, fibers, and other bulk structures. If the nanoparticles stick together and flocculate they cannot be processed. A schematic of the various interaction forces that are relevant on the nanoscale is shown in Figure 1. Clearly scientific under-
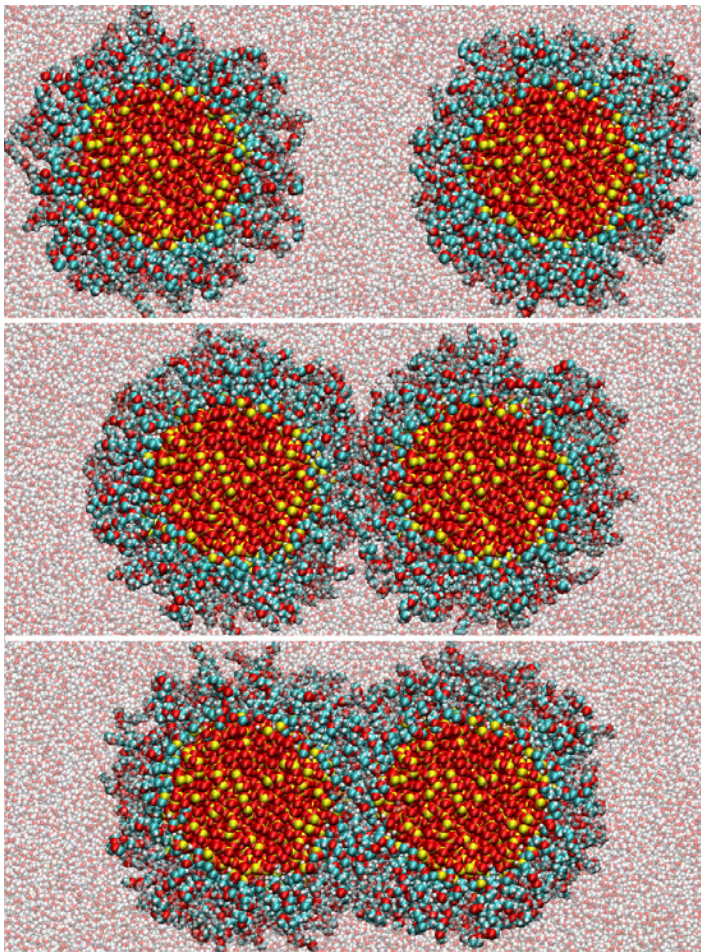
Figure 2: Polyethylene coated silica nanoparticles in water at three separations. Silica core of nanoparticle is 5 nm in diameter. Courtesy of J. Matthew Lane.

Figure 3: Snapshot of ellipsoidal nanoparticles (red) at 20% volume fraction in solvent (blue). Courtesy of W. M. Brown.

standing at multiple length scales, from atomistic to continuum, is crucial to surmounting these challenges in designing and manufacturing nanocomposite materials.

To achieve a stronger scientific understanding of the factors that control nanoparticle dispersion and rheology we are developing a multiscale modeling approach which will bridge scales between atomistic and molecular-level forces active in dense nanoparticle suspensions. At the atomic scale, we are carrying our molecular dynamics simulations with full atomistic detail to determine the interparticle forces between nanoparticles of various sizes and coatings. The solvation (velocity independent) and hydrodynamic (velocity dependent) forces are determined by moving two nanoparticles together at a given velocity as illustrated in Figure 2 for two polyethylene coated silica nanoparticles in water. To study the effect of particle shape on rheology we are simulating ellipsoid nanoparticles as shown in Figure 3.

At the meso-scale, a coarse-grained solvent model is being used to capture hydrodynamic effects. The interparticle forces determined from these simulations will be used in large-scale continuum flow solvers to model the rheological response and dispersion characteristics typical in a processing flow. The aim of our research and development is to achieve a unique meso-scale modeling and simulation tool-set designed to predict the key underpinning phenomena of nanoparticle suspension rheology and stability.

Atomic Simulation Guides Nanomechanics Theory
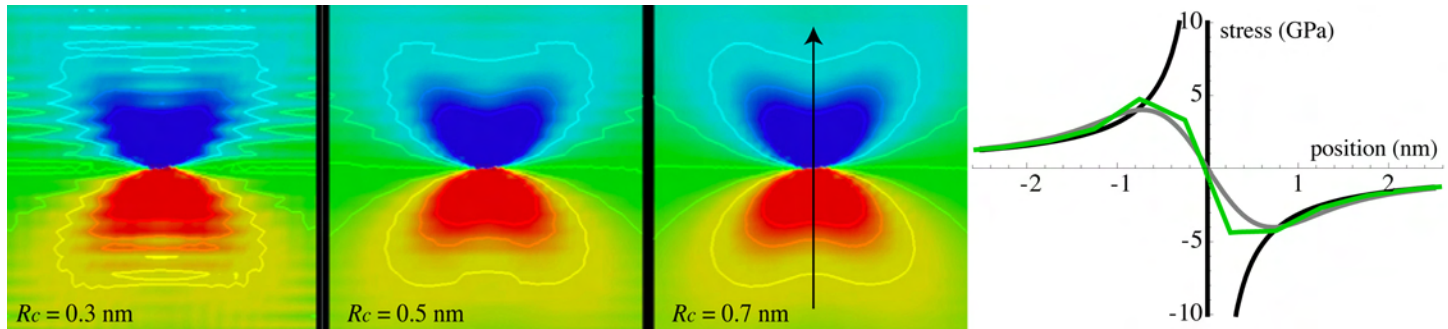
Figure 1: Left: Stress field around a dislocation core showing regions of compressed (blue) and stretched (red) crystal. As the spatial averaging volume size is increased from 0.3 to 0.7 nm, contours of constant stress become more continuous. Right: Stress as a function of position along the line shown for a 0.7 nm averaging volume. Local elasticity theory (black) fails to properly describe stress within a 2 nm region surrounding the defect while non-local elasticity (grey) — fit to atomistic simulation (green) — does.

Nanoscale stresses at defects require new theoretical approaches

For more information:
Technical Contacts:
Edmund B. Webb III
505-284-6517
ebwebb@sandia.gov

Jonathan A. Zimmerman
925-294-2437
jzimmer@sandia.gov

Science Matters Contact:
Alan Burns, Ph.D
505-844-9642
aburns@sandia.gov

Continuum theory has been used for decades to analyze and predict the mechanics of materials and structures as diverse as airplanes to prosthetics. However, as existing and emergent technologies shrink to the nanometer range, quantities such as stress and strain become ill defined and the application of continuum mechanics in nanomechanical frameworks becomes suspect. Manufacturing implications are significant; for example, traditional design tools do not accurately apply to microscale or nanoscale electro-mechanical systems because continuum mechanics concepts, on which those design tools are based, do not apply on such length scales. While modeling and simulation methods (e.g., molecular dynamics) have provided a wealth of information for such systems, connections to engineering scale analysis are not clear.

Researchers at Sandia have been investigating and refining definitions for continuum variables at the atomic scale. The result is that quantities inherent to atomistic simulation, such as atom positions, velocities and inter-atomic forces, can be used to determine spatially varying stress fields. These definitions effectively overlay a continuum representation on an atomistic

system. Weighted spatial averages of atom quantities within finite-sized volumes are used to estimate stress at the material points corresponding to those volumes. Time averaging these estimates permits meaningful comparison to continuum theory. For example, analysis of an edge dislocation in a crystal (an imperfection in the local ordering of the crystal's structure) reveals that averaging volumes surrounding continuum material points must be of a minimum dimension (~ 0.7 to 1.0 nm) in order for stress fields to be resolved in a continuous fashion (Fig. 1). This analysis also shows that variation of stress close to the dislocation core (or center) is not well represented by conventional local elasticity theory, but rather by more advanced non-local theory. Most significantly, marrying non-local elasticity theory to atomistic simulation permits direct determination of length scale parameters that achieve accurate description of the stress surrounding the material defect. Thus, atomistic simulation employing newly defined mechanics variables can be used to develop robust nanomechanics theory.

Atomistic-based expressions for stress were used to gain fundamental understanding of materials behavior:
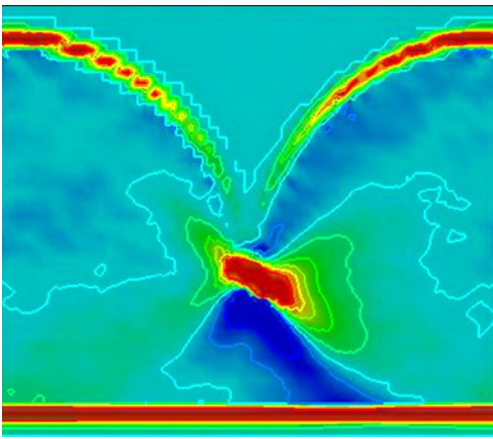
Figure 2: Results from a molecular dynamics simulation are used to predict the stress field during the initial coalescence of growing islands (a two dimensional cross-section is shown from a three dimensional simulation). Tensile stress (red) is concentrated within the coalescence region, signifying the formation of a dislocation defect. Also discernable is tensile stress that occurs at the island surfaces, tensile stress near the substrate's bottom free surface and compressive stress (blue) that exists within a majority of the volume of the islands (due partly to surface curvature effects).
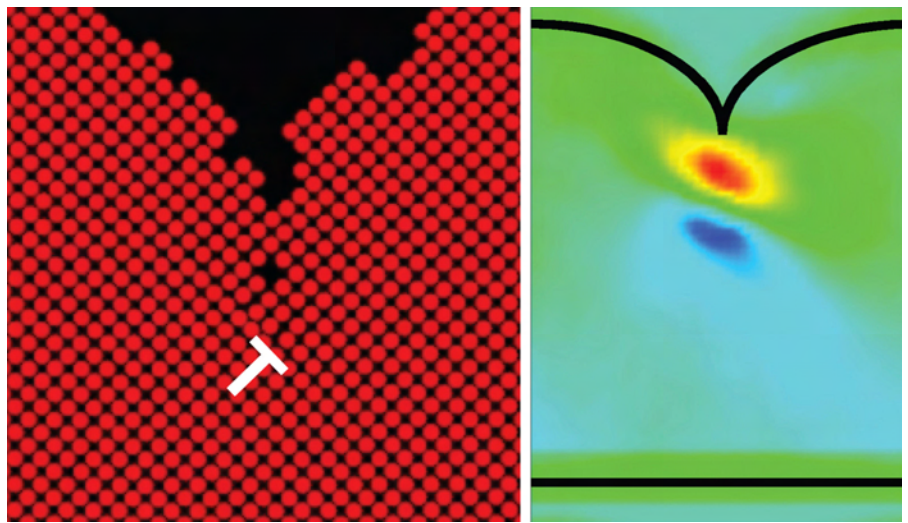
Figure 3: Results from a molecular dynamics simulation are used to show the formation of a defect (left) and the evolution of stress (right) that occurs during ongoing coalescence of islands in a growing film (two dimensional cross-sections from three dimensional simulations are shown). For clarity, a white 'T' is placed at the location where the defect is formed while black lines show the approximate locations of the islands' free surfaces and the substrate's bottom free surface.

specifically, stress evolution during metallic thin film growth. During such growth, isolated islands are first nucleated, and then proceed to coalesce and form continuous planar films. While experiments have successfully quantified the average stress within a film during growth, little is known about the distribution of stress within a film or whether defects form as island coalescence occurs. Molecular dynamics simulations confirmed suppositions from experiment that coalescence happens in two stages: initial coalescence occurs when neighboring islands first join together. At that point a dislocation defect is formed and a concentration of tensile stress exists within the coalescence region (Fig. 2). After initial coalescence, ongoing coalescence is exhibited and new defects are periodically formed. While this ongoing coalescence stage reduces system energy through the elimination of surfaces, tensile stress continues to increase during defect formation events (Fig. 3). Such nano-mechanical analysis can provide guidance on choosing growth conditions that lead to films of specific morphology and structure.

References:

Edmund B. Webb III, Jonathan A. Zimmerman and Steven C. Seel, "Reconsideration of Continuum Thermomechanical Quantities in Atomic Scale Simulations", *Mathematics and Mechanics of Solids*, **13** (2008) 221-266

J.A. Zimmerman, P.A. Klein and E.B. Webb III, "Coupling and communicating between atomistic and continuum simulation methodologies", Multiscaling in Molecular and Continuum Mechanics: Interaction of Time and Size from Macro to Nano, pp. 439-455, Springer, The Netherlands – Spring, 2007

Steven C. Seel, Jeffrey J. Hoyt, Edmund B. Webb III and Jonathan A. Zimmerman, "Modeling metallic island coalescence stress via adhesive contact between surfaces", *Physical Review B*, **73** (2006) 245402

J.A. Zimmerman, E.B. Webb III, J.J. Hoyt, R.E. Jones, P.A. Klein and D.J. Bammann, "Calculation of stress in atomistic simulation", *Modeling and Simulation in Materials Science and Engineering*, **12** (2004) S319-S332

Materials Science and Technology
Nanoscience

Probing the evolution and stability of thin ice films on solids with molecular-layer resolution.
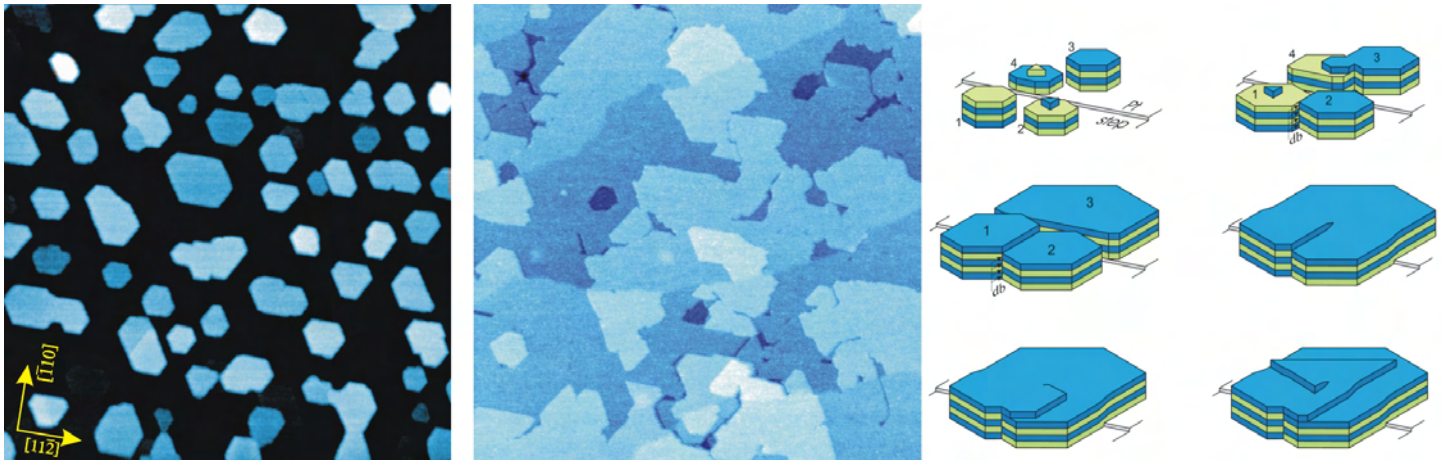
Figure 1: The two 500×500 nm^2 STM images (left and center) of ice films grown on Pt(111) at 140 K demonstrate the capability of STM to investigate ice multilayers nondestructively. Left: 0.8 nm thick ice film with individual $\approx$3 nm high crystallites. Center: 4 nm thick continuous ice film. The abrupt contrast changes are ice surface steps of molecular height, which have never been imaged before. Right: schematic of a coalescence scenario leading to cubic-ice formation.

Scanning tunneling microscopy is used to decipher what governs the morphology and structure of ice films.

For more information:
Technical Contacts:
K. Thürmer
925-294-4564
kthurme@sandia.gov

N.C. Bartelt
925-294-3061
bartelt@sandia.gov

Science Matters Contact:
Alan Burns, Ph.D
505-844-9642
aburns@sandia.gov

The interaction of water with solid surfaces plays a key role in applications like catalysis, corrosion, water purification and fuel cells. It is also important in many natural processes that occur in the earth's atmosphere or in the outer solar system. For example, rainfall is triggered by nucleation of ice crystals on micron-sized particles in clouds. Despite its importance, little is known about water-solid interactions. In fact, to this day, the best theoretical models fail to reproduce even the most basic phenomena.

Two examples of basic unsolved questions concern the growth of ice on metals. First-principles calculations predict that ice forms 3D crystals that grow directly on the bare metal substrate, whereas multiple experiments indicate that water first forms a molecularly-thin wetting layer on which 3D crystals grow. Settling this discrepancy could provide much insight into ice-film energetics in particular or water-solid interaction in general. Another basic unsolved question concerns the metastable, low-temperature phase of cubic ice, which had been discovered in the 1940's, but whose origin remains puzzling.

Electron microscopy techniques have been powerful in solving similar puzzles for metal growth; however, they all failed in studying multilayer ice because the imaging electrons immediately damage the insulating ice. Up to now, scanning tunneling microscopy (STM) has also not been successful because it requires an electric current to flow between STM tip and sample, and ice generally cannot supply the electrons needed for imaging. However, at Sandia we recently discovered conditions where the needed electrons are extracted from the ice valence band, thus making nondestructive imaging possible.

Figure 1 illustrates the success of this novel approach. The left picture shows a 0.8 nm thick ice film grown on a Pt substrate at 140K. Individual nanometer-sized ice crystals are embedded in a molecularly-thin wetting layer (black). Upon depositing more water, these crystals coalesce into a
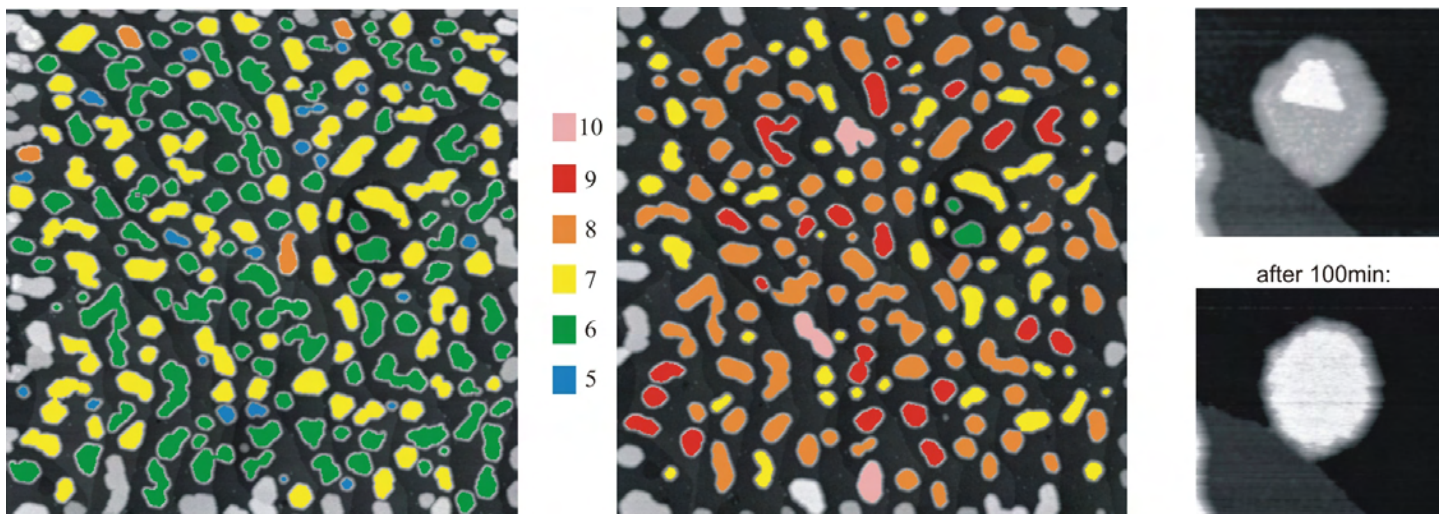
Figure 2: Nucleation-limited dewetting. Left: 1×1 μm² image of an 0.8 nm thick ice film grown at 140 K with the height of each three-dimensional crystallite colored differently. The colors represent the height in molecular layers of ice (one layer = 0.37nm). Center: Image of the same surface region after annealing at 140 K for one hour. Right: individual nucleation event.

continuous film at around 4 nm average thickness (center picture). By deciphering the exact nature of this coalescence we are able to determine the origin of the metastable cubic ice. It is steps in the substrate that modify how the molecular layers of merging crystallites connect. As a result, screw dislocations are created that, in turn, form growth spirals where cubic ice is being produced.

To probe the stability of the ice film, we monitored changes in morphology when the 0.8 nm thick film is annealed for 1 hour at 140K. The image sequence in Figure 2 reveals that the ice crystals grow thicker and consequently expose more of the wetting-layer covered Pt surface. The results show that it is the rate at which new layers nucleate, and not diffusion along the surface, that determines how fast individual crystallite shapes equilibrate. Applying nucleation theory to measured growth rates vs. crystallite dimensions, we obtain new bounds on the energetics both of step formation on ice and of the Pt-ice interface.

This new insight into ice-film energetics provides a benchmark against which first-principles calculations can be further tested and enhanced. Improving the still unsatisfactory theoretical models would help address a variety of unsolved questions in the general field of water-solid interactions.

References:

K. Thürmer and N.C. Bartelt, "Growth of multilayer ice films and the formation of cubic ice imaged with STM", Physical Review B **77**, 195425 (2008).

K. Thürmer and N.C. Bartelt, "Nucleation-limited dewetting of ice films on Pt(111)", Physical Review Letters **100**, 186101 (2008).

Materials Science and Technology
Nanoscience

Toward Three-Dimensional Nanoengineering of Heterogeneous Catalysts
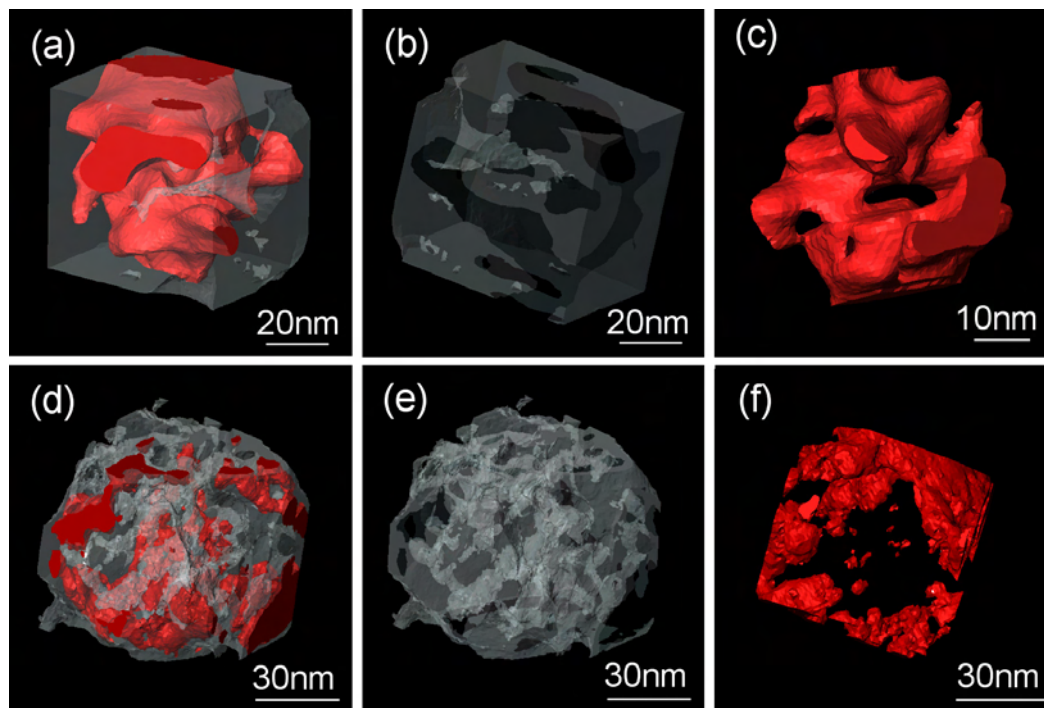
Figure 1: 3-D reconstructions of the two catalysts. (a)-(c) shows the Co_3O_4/γ-alumina system, and (d)-(f) shows the Co_3O_4/Ni-aluminate/α-alumina system. (a) shows the Co_3O_4 in red and the γ-alumina in semi-transparent grey. (b) shows only the alumina, rotated 180° with respect to (a). The darker grey areas indicate the porous regions in which the cobalt oxide resides. (c) shows that agglomerates of the cobalt oxide particles are also very porous. (d) shows Co_3O_4 in red on a Ni-aluminate cluster in semi-transparent grey. (e) shows only the highly porous Ni-aluminate and (f) shows that despite this porosity, the cobalt oxide chooses to stay primarily on the surface and form "nanocages."

3-D nanoscale structures correlate with higher selectivity of catalysts

For more information:

Technical Contact:
Ilke Arslan
925-294-1469
iarslan@sandia.gov

Science Matters Contact:
Alan Burns, Ph.D
505-844-9642
aburns@sandia.gov

The Fischer-Tropsch (FT) process is a key industrial process that has a long history of commercial development and application in the conversion of coal and natural gas to clean hydrocarbon fuel. The importance of FT technology is emphasized by increasing crude oil prices, the need to diversify energy sources with minimum environmental impact, and explore sustainable sources such as biomass. As such, FT catalysts are widely studied by oil companies, labs, and universities around the world. FT catalysts based on cobalt particles on a porous alumina support provide high activity and selectivity to long chain paraffins, low-water-gas shift activity, and economic viability in converting a variety of hydrocarbon sources to fuel and petrochemical products.

To optimize the efficiency of these catalysts and the FT process, a fundamental understanding of the their size, shape, and distribution, and their relation to catalytic activity/selectivity must be obtained on the nanoscale. Standard methods for measuring particle size and dispersion, such as chemisorption and X-ray diffraction (XRD), generate average microscopic properties and give little direct information. In contrast, the transmission electron microscope (TEM) is a powerful tool for the direct study of the catalyst particles on the nano and atomic scale. However, since cobalt oxide particles are known to aggregate in three-dimensions, a simple two-dimensional TEM image is not sufficient to completely describe their structure. Advances in electron tomography in the scanning transmission electron microscope (STEM) now enable reliable and quantifiable three-dimensional reconstructions of inorganic materials to be achieved with a spatial resolution approaching 1nm^3. Here we apply this technique to two Re promoted

Sandia National Laboratories

FT catalyst systems: the first is a 20 wt% Co/0.5 wt% Re catalyst on a high surface area γ-alumina substrate, and the second is a 12 wt% Co/0.5 wt% Re catalyst on a heat-treated substrate of α-alumina impregnated with 5% Ni. The heat treatment and addition of Ni in this latter system acts to strengthen the support and thus provides superior mechanical properties. The materials were studied in their unreduced condition so that Co is present in the form of Co_3O_4. The C_5+ selectivity of the second system is greater than the first by ~5%, and while this appears moderate, the difference will be of clear significance in a commercial system.

The first and less selective catalyst is shown in Figure 1(a-c). In this system, the cobalt oxide enters the highly porous γ-alumina support and completely fills the pores, forming an interlocking catalyst/support structure. Even in a reduced state, this morphology is expected to yield very little physical space for reactions to take place. In the second and more selective system (Figure 1(d-f)), the cobalt oxide preferentially sits solely on the Ni-aluminate (which in turn connects to α-alumina pieces, not shown in this figure), and does not penetrate the pores at all, instead forming nanocages. This unexpected Co_3O_4 distribution provides a more open local environment for reactions to take place, and we believe that the higher selectivity of this catalyst system over the other correlates with the 3-D nanocage morphology and its selection of the Ni-aluminate support over γ-alumina. This powerful 3-D information gives us direct insight into the nanoscale differences between catalyst systems that are invisible to bulk property measurements.

The ability to understand and optimize parameters that influence specific properties, such as selectivity, is of tremendous potential for the future design of heterogeneous catalysts that play a key role in the management of energy supply for hydrocarbon production with a positive environmental impact. We are also using these powerful 3-D techniques to study a variety of complex nanomaterials, such as porous nanoparticles made of Pd, Pt, Au, C, and C nanotubes with applications in hydrogen and electrical energy storage, and multi-shell semiconductor nanowires with applications in optoelectronic nanodevices.

Reference:

"Toward Three-Dimensional Nanoengineering of Heterogeneous Catalysts," I. Arslan, J. C. Walmsley, E. Rytter, E. Bergene, and P. A. Midgley, *Journal of the American Chemical Society*, **130 (17)**, 5716-5719 (2008).

Materials Science and Technology
Nanoscience

Mid-infrared Electroluminescent Quantum Dots

Figure 1: InAs quantum dots can be grown on the surface of GaAs, and then imaged using atomic force microscopy microscopy (AFM). This technique can be used both for verifying the size of the dots (about 20 nm), as well as the density of dots per unit area. For illustrative purposes, the ground (blue) and excited state (white) electron wave functions are drawn schematically within the quantum dot AFM image.
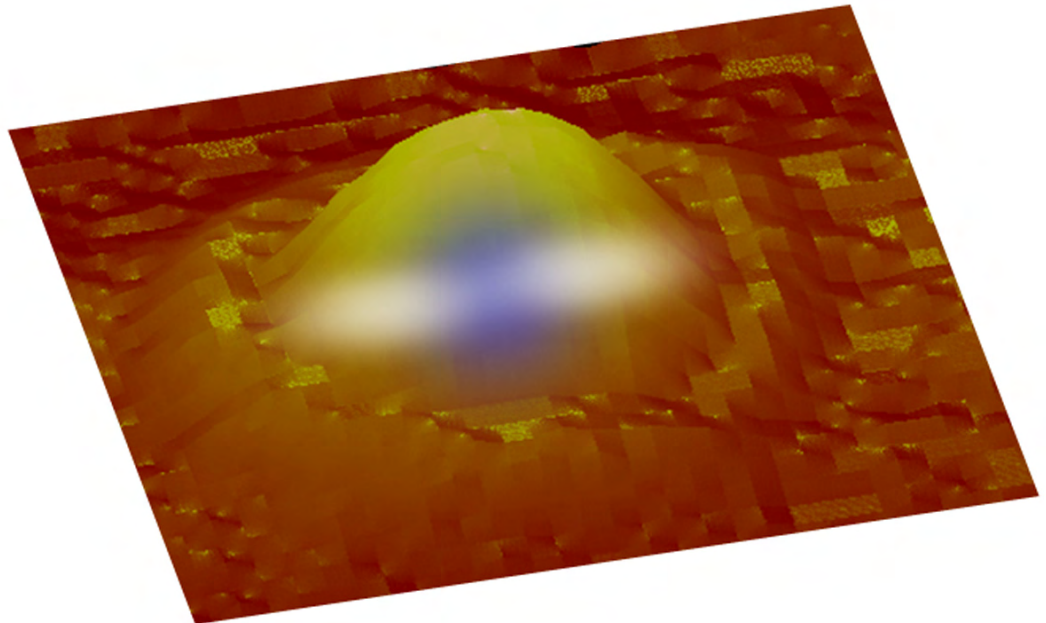
Engineering the layers around quantum dots can greatly impact performance

For more information:
Technical Contact:
Eric Shaner
505-284-5636
eashane@sandia.gov

Science Matters Contact:
Alan Burns, Ph.D
505-844-9642
aburns@sandia.gov

Compact sources of mid-infrared (mid-IR, 3 µm -12 µm) radiation are important to defense, health monitoring, and environmental sensing. While quantum cascade lasers (QCLs) have been revolutionary over the past decade in covering the mid-IR, there is still considerable room for improvement in terms of wall-plug efficiency. One path to improve conversion of electrical power into light is to reduce non-radiative losses by utilizing three-dimensional nanostructures such as InAs quantum dots.

While the semiconductor quantum dot approach is still in its relative infancy compared to the mature quantum well based QCLs, recent progress has been made by researchers at Sandia, in collaboration with the University of Massachussetts Lowell, that demonstrates the potential of this technology. InAs quantum dots are grown in the GaAs material system through a process known as 'self-assembly.' These lens-shaped 'artificial atoms' (figure 1) are approximately 2 nm tall with a 20 nm base. It turns out that the energy separation between the ground (s) and first excited (p) electron state in these structures corresponds to wavelengths ranging from roughly 8 µm (155 meV) to 14 µm (90 meV), depending on size. In order to electrically pump the dots, electrons need to first be injected into the upper p-state through a quantum tunneling process. Once an electron is in the excited state of the dot, it can either transition to the lower energy s-state and tunnel out of the dot, emitting a photon along the way, or tunnel directly out of the dot without emitting a photon. It is the control of this process, through properly designed electron filtering, that primarily determines the efficiency of quantum dot based emitters.

Sandia National Laboratories

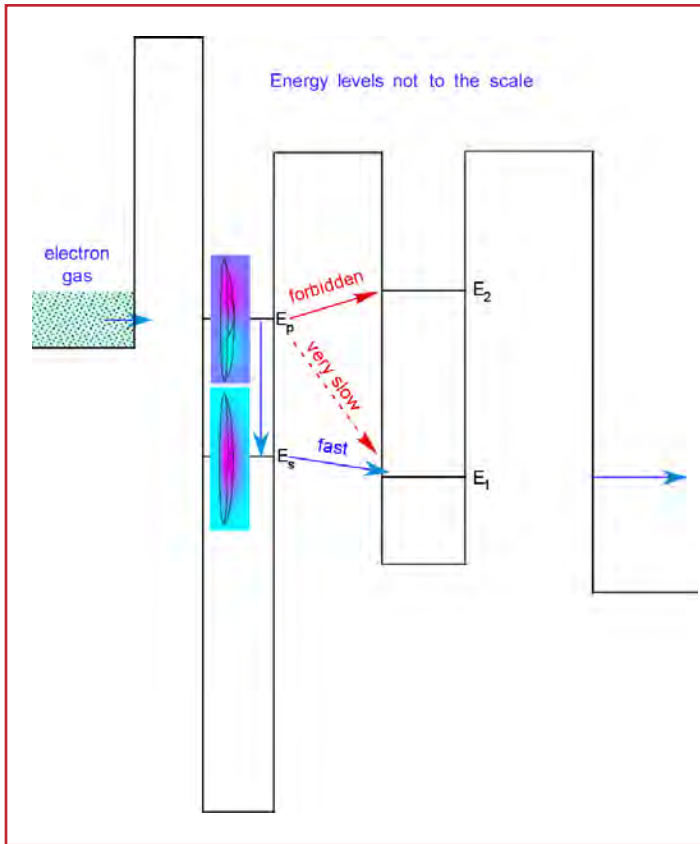**LDRD** LABORATORY DIRECTED RESEARCH & DEVELOPMENT

Figure 2: Basic description of the quantum dot design rule implemented in this work. The quantum well filter is designed in such a way that the upper p-state in the dot is positioned energetically below the second quantum well level, while the low s-state in the dot is positioned slightly above the first quantum well state.
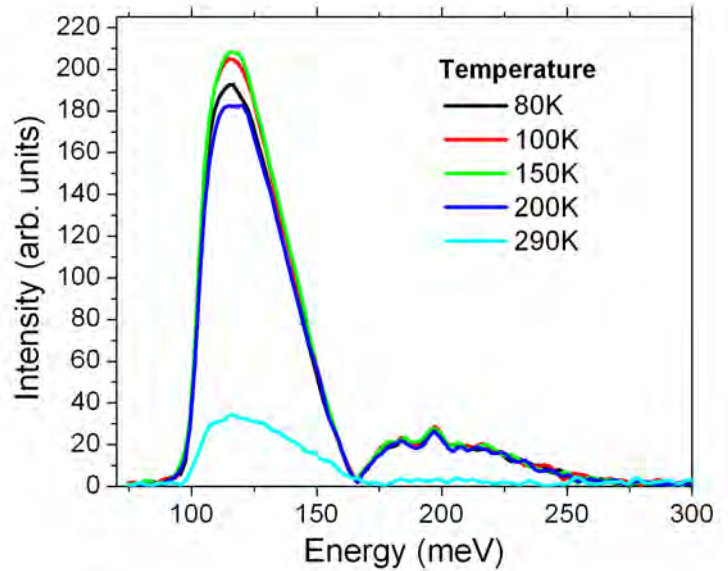

Figure 3: Emission spectra of electrically pumped quantum dot material. Up to 200K in temperature, the emission is relatively unchanged. At room temperature, the peak intensity at 120 meV is down to approximately 15% of its low temperature value, but emission is still observed.

In QCLs, it is common to design structures where active region energy states are aligned to filter states in order to control photon emission and electron extraction from the active region. Until recently, an appropriate design rule to guide filter design did not exist for quantum dots. While it might seem like a similar problem to align energy states between the dot and filter stage, it turns out this is not the ideal condition. Instead, the ground state and excited state of the dot need to be intentionally mis-aligned (figure 2), such that the ground state lies slightly above the filter extraction state, and the excited p-state lies just below the next available tunneling state. This divergence from QCL architecture arises from differences in dot-to-well electron tunneling compared to QCL well-to-well transitions.

The end result of this new design is electrically pumped quantum dot material that emits up to room temperature (figure 3). Previous iterations of this material design, with a non-optimized quantum well filter, exhibited reduced performance and only worked at cryogenic temperatures. While research still needs to be done in order to obtain gain/lasing action in this material, this result is intriguing as it demonstrates that engineering the layers around the quantum dots can greatly impact performance. Unlike well-based QCLs, mid-IR quantum dots can naturally emit light normal to the surface. This makes them ideal candidates for surface emitting sources as well as enabling their integration into high-Q photonic cavities to enhance output and tune emission wavelength. This advantage also opens up the possibility for quantum dots as mid-IR single photon sources for quantum communications.
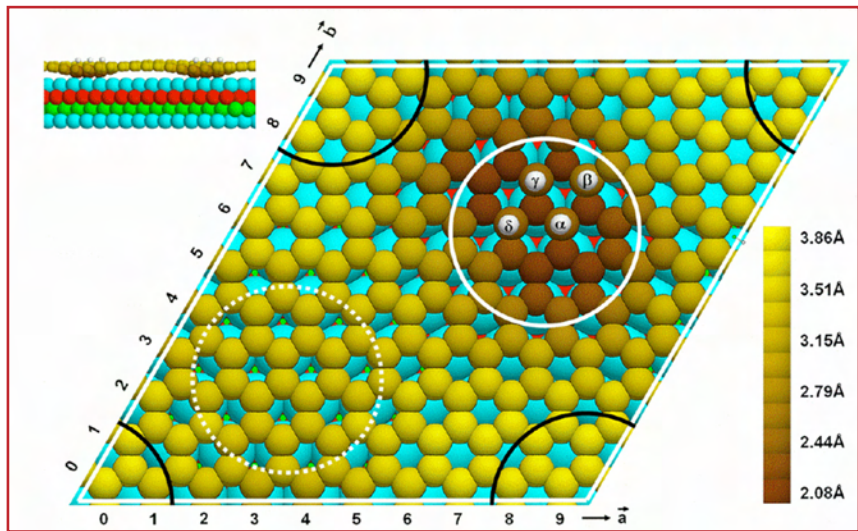
Materials Science and Technology
Nanoscience

How an ordered nanoparticle array can grow on a "featureless" surface
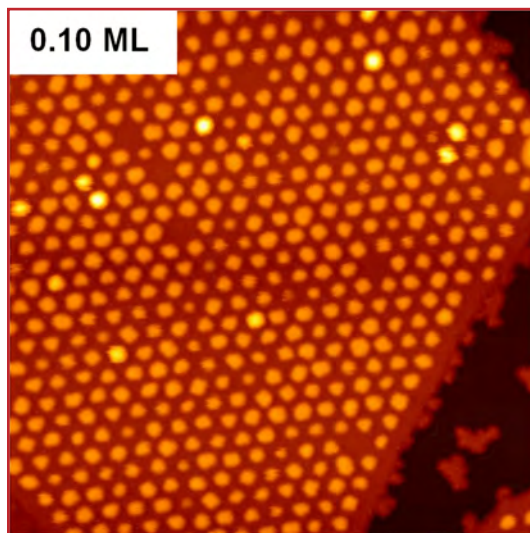
Figure 1: STM image of a periodic array of iridium clusters formed by depositing 1/10 monolayer iridium on a graphene flake (prepared by pyrolysis of ethylene) on an iridium surface (after Ref. 1).

Figure 2: Computed atom arrangement for a cluster in a region where the carbon flake can buckle (after Ref. 2). Carbon atoms are color coded according to their heights above the iridium surface atoms (cyan). In the "bad" regions surrounded by black arcs, no carbon atoms lie directly above surface iridium atoms. The iridium atoms of the cluster (α, β, γ and δ) are colored white and drawn as small balls to show where they sit on the carbon sheet.

By buckling, a carbon–atom sheet both attaches firmly to an iridium crystal, and organizes iridium atoms deposited on it into a periodic cluster array.

Periodic arrangements of transition-metal clusters on surfaces offer exciting prospects for catalysis, information storage and quantum computing. Periodicity may result from cluster-cluster interactions, but a thermally stable array is likelier if a surface presents a periodic arrangement of exceptionally attractive sites to deposited atoms.

Sandia research has explained a subtle example, the iridium cluster array grown, and stable to 400 - 500K, on a single, carbon-atom layer (a "graphene" flake) on the smoothest of iridium metal's crystal surfaces (see Fig. 1). This advance was the fruit of an ongoing collaboration with university researchers in Germany. A new idea was needed because a graphene layer is essentially flat, and, as one knows from the low friction of graphite (which is a stack of graphene layers), typically interacts weakly with its surroundings. What could enable a flat graphene flake on a seemingly featureless iridium surface to organize deposited atoms into a periodic cluster array?

Our answer traces back to the differing radii of carbon and iridium atoms, which imply that carbon atoms only lie directly above iridium atoms in certain regions of a graphene flake on the iridium surface – regions that form a periodic array (Fig. 2). Computational simulations show that these regions are favorable for a buckling of the flake, which bonds it strongly to the underlying metal, and at the same time to iridium atoms deposited on top of it. The carbon atoms lying directly above iridium atoms of the metal surface move downward to form strong bonds to them. Alternate carbon atoms move upward, capturing deposited iridium atoms into a cluster.

Sandia National Laboratories

NNSA National Nuclear Security Administration

The remarkable pinning effect is shown in Fig. 3. Before any iridium is deposited on it (upper panel), the carbon flake is virtually flat, and weakly attached to the underlying metal. Around clusters at favorable sites, the carbon flake is depressed into contact with the metal, and binds strongly to it. Moving clusters to unfavorable regions (cf. Fig. 2), their attachment to the flake, and the flake's attachment to the metal become weak, as the flake no longer buckles. For this reason, experimentally, clusters are not observed in the unfavorable sites.

The mechanism that gives rise to cluster arrays in the iridium on graphene on iridium metal system is sufficiently general that one can expect similar 'templating' to occur if different elements are substituted for the underlying metal and the clusters. This suggests that graphene supported cluster arrays will afford the possibility of wide ranging, highly controlled studies of catalytic chemistry. With magnetic clusters substituted for iridium, one also contemplates the possibility of novel data storage and perhaps quantum computational applications.

References:

1. A. N'Diaye, S. Bleikamp, P. J. Feibelman, T. Michely, Phys. Rev. Lett. **97**, 215501(2006).

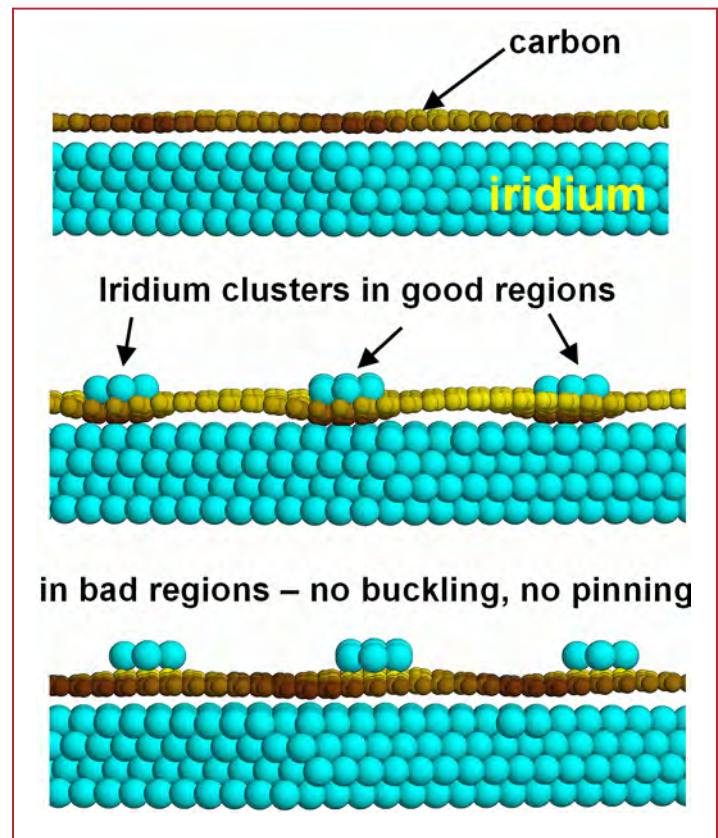2. P. J. Feibelman, Physical Review **B77**, 165419(2008).

For more information:

Technical Contact:
Peter J. Feibelman
505-844-6706
pjfeibe@sandia.gov

Science Matters Contact:
Alan Burns, Ph.D
505-844-9642
aburns@sandia.gov

**Figure 3:** With the sizes of the balls representing carbon and iridium atoms sized proportionately to their radii, and balls, side views show: a carbon flake "floating" above the metal (upper panel), a buckled carbon flake pinned to the metal, with an array of iridium clusters strongly attached to it (middle panel), and a floating carbon flake, with iridium clusters sited in unfavorable regions (bottom panel).

Materials Science and Technology
Optical Sciences

Microlasers
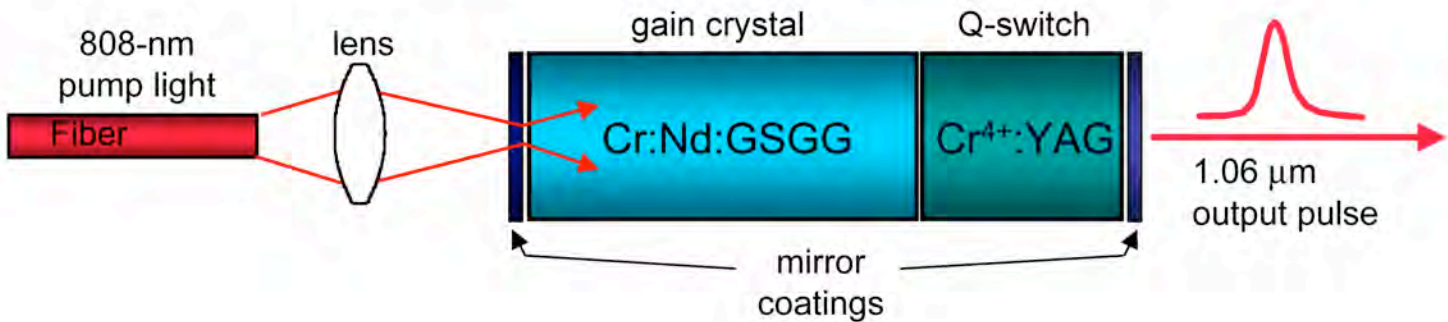
Figure 1: Schematic diagram of a laser-diode-pumped microlaser. Pump light from a fiber-coupled laser diode is imaged into the end of the microlaser. The microlaser consists of a gain crystal bonded to a passive Q-switch crystal. The end faces are polished flat and parallel and mirror coatings are deposited directly on the faces to form a monolithic laser cavity.

Versatile lasers fill unique requirements in many diverse applications

Diode-laser-pumped passively Q-switched microlasers are efficient, rugged, and compact lasers that have become critical components in Sandia's programs in optical-based firing sets, remote sensing (LIDAR, LIght Detection And Ranging), molecular spectroscopy, and other applications.   For example, microlasers can be used to optically trigger high-voltage switches in firing sets, thereby providing improved safety from lightning and static discharge. Also, microlasers enable extremely compact LIDAR systems which can be used to map the size, shape, location, and composition (via spectroscopic signals, such as absorption, Raman scattering and laser induced fluorescence) of clouds or aerosols. Other potential applications include using microlasers in very compact laser ranging (LADAR, LAser Detection And Ranging) instruments. LADAR detects hard-target backscatter from solid objects, and is used for determining range to targets or 3-D imaging of remote scenes.

A typical microlaser, illustrated in Figure 1, is pumped from one end by a laser diode (often fiber coupled) to maximize the spatial overlap between the pumped volume and the lasing mode and thereby maximize its overall efficiency. The microlaser itself consists of a gain crystal (Cr:Nd:GSGG in this example) diffusion bonded to a saturable absorber crystal (Cr^{4+}:YAG for 1-µm-output lasers) that serves as a passive Q-switch. Both end faces of this composite crystal are polished flat and parallel to one another with dielectric mirror coatings on the faces to form a monolithic laser cavity. When the laser is pumped, the saturable absorber prevents laser oscillation until the gain in the laser crystal is high enough to saturate the absorbing transition, resulting in the emission of a short (~1-ns-long) Q-switched pulse of light. These miniature passively Q-switched lasers can be operated single-shot or repetitively pulsed at rates exceeding 20 kHz.

The versatile miniature lasers have been designed to produce nanosecond-long optical pulses with excellent beam quality and high spectral purity that are ideal for efficient nonlinear optical frequency conversion to the ultraviolet or the infrared, enabling the miniaturization

For more information:
Technical Contact:
Randy Schmitt
505-844-9519
schmitt@sandia.gov

Science Matters Contact:
Alan Burns, Ph.D
505-844-9642
aburns@sandia.gov

Sandia National Laboratories

LDRD
LABORATORY DIRECTED RESEARCH & DEVELOPMENT

Figure 2: Examples of Sandia-designed microlasers. The microlaser on the left is a Nd:YAG laser designed to produce high-energy (>200 μJ/pulse) single-frequency output for spectroscopic applications. The microlaser on the right is a Cr:Nd:GSGG laser which is fabricated from radiation-hard materials and is intended for weapons applications such as optical triggering of sprytrons.

of spectroscopic-based instrumentation and compact LIDAR systems. Many of the microlasers have output wavelengths, pulse energies, and pulse durations that are not available commercially, but are required and optimized for specific Sandia applications. For example, we designed and built a microlaser from radiation-hard Cr:Nd:GSGG and Cr^{4+}:YAG for optically triggering sprytron tubes with with as little as a few microjoules of Q-switched laser energy. This microlaser, shown in Figure 2, may eventually be engineered into an all-optical firing set, leading to improved safety of weapons firing systems from lightning and static discharge. We are also exploring using microlasers to directly initiate explosive materials. potentially eliminating the need for an electrical detonator altogether.

We have also developed a single-longitudinal-mode, high-energy (up to 200 μJ/pulse) Nd:YAG microlaser (also shown in Figure 2) for use in compact spectroscopic-based instrumentation. The 1064-nm output from this microlaser has been efficiently converted to 355 nm and 266 nm for use in laser-induced-fluorescence instruments used for research on detection of biological aerosols and other materials. This same microlaser has been frequency converted to 3.27 μm for use in a hand-held methane imager designed for short-range (1- 2 m) standoff detection of leaks in natural gas plumbing. Here, the laser was optimized to operate in a double-pulse mode, emitting a pair of 2-ns-long pulses separated by 100 μs (with an overall repetition rate of ~2 kHz) as required to perform a differential absorption measurement.

As part of a fiber laser project, we developed a family of Yb:YAG microlasers with pulse lengths from 0.5 ns to 1.0 ns and single-longitudinal-mode operation at repetition rates up to 19.4 kHz to use as seed sources for Yb-doped fiber amplifiers. The 1030-nm output of Yb:YAG more closely matches the gain peak in Yb-doped fiber than the ~1060-nm output of Nd-based lasers and results in more efficient pulsed fiber laser systems. Using the 1030-nm microlaser as a seed source, we demonstrated a 40% increase in pulse energy compared with 1062.4-nm source typically used.

As the demand for more compact and field-able laser-based instrumentation increases, the need for more specialized microlasers will also increase. Sandia will continue to lead in developing microlasers to meet the unique needs of research and development of optical firing sets, miniature sensors, and other national security applications.
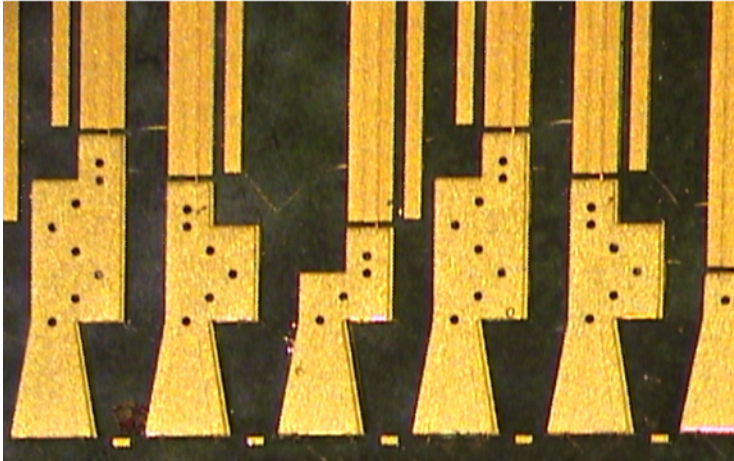
References:

R. L. Schmitt, *"Monolithic passively Q-switched Cr:Nd:GSGG microlaser,"* Proc. SPIE, **5871**, 587105 (2005).

R. L. Schmitt and B. T. Do, *"Design and Performance of a High-Repetition-Rate Single-Frequency Yb:YAG Microlaser,"* Proc. SPIE, **6871**, 687105 (2008).
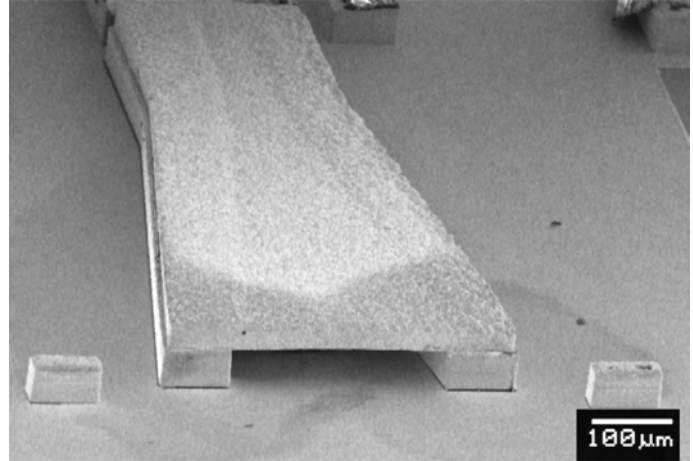
Microelectronics and Microsystems
Photonics

Terahertz devices

Figure 1: Collection of completed rectangular waveguides integrated with THz QCLs on a single chip. The lasers (the straight wider lines extending off the top), penetrate a little distance into the hollow waveguides (at the bottom).

Figure 2: Close-up, scanning electron microscopy image of a terahertz (THz), rectangular, metal-waveguide horn antenna formed over a THz semiconductor laser mounted to the chip. The flare of the horn improves the spatial pattern of the emitted THz radiation.

From vacuum tubes to solid state

*For more information:*
Technical Contact:
Michael C. Wanke
505-844-2532
mcwanke@sandia.gov

Science Matters Contact:
Alan Burns, Ph.D
505-844-9642
aburns@sandia.gov

The range of frequencies around 1 terahertz (THz = 10^{12} cycles per second) is like the neglected middle child in the electromagnetic spectrum. Both microwave (below roughly 0.1 THz) and infrared (above roughly 20 THz) are used widely, thanks to a high performance, mass-produced semiconductor technology base. Caught in between, THz radiation lacks the microelectronic foundation of its spectral siblings and still relies to a great extent on large-scale tube-based components analogous to using vacuum tubes for radios. Nonetheless, there has been broad interest in exploiting the THz spectrum. Laboratories worldwide have carried out proof-of-principle demonstrations showing how THz is far more effective than microwave or infrared in very rapid and highly precise hazardous chemical sensing and identification, concealed threat detection and imaging, noninvasive medical and biological diagnostics, and secure high-speed telecommunications. To get such THz applications out of the laboratory and into widespread use will require bringing THz into the solid-state era.

Sandia researchers recently took a major step along an innovative route towards a THz microelectronic technology base. The Sandia team, working under a Grand Challenge project, demonstrated the first successful integration of a THz quantum cascade laser (QCL) with a micro-machined gold rectangular waveguide, all on a semiconductor chip (Fig. 1). QCLs have been researched and developed extensively at Sandia and are the only solid-state source capable of producing more than a few milliwatts of coherent average power between 1 to 5 THz. Unfortunately, QCLs generate highly divergent and non-uniform radiation beam patterns into free space that curtail their usefulness in practical applications. The solution pioneered by Sandia forces a QCL to radiate into a three-dimensional waveguide structure (Fig. 2) in such a way that the THz electromagnetic field is guided and shaped by the waveguide boundaries in a simple and predictable manner that can ultimately be manipulated by standard waveguide design techniques.

Sandia National Laboratories

LDRD
LABORATORY DIRECTED RESEARCH & DEVELOPMENT
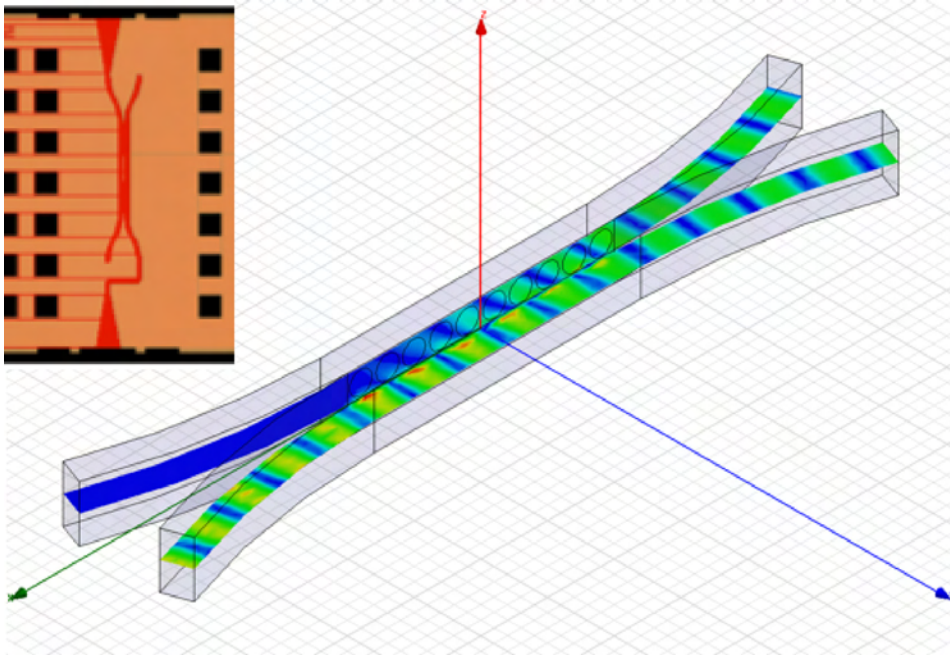
Figure 3: (Left) THz rectangular waveguide coupler device. (Right) Results of electromagnetic modeling of the device performance.

The integration of QCLs and waveguides on a chip posed significant technical challenges stemming from the small cross-sectional dimensions of the QCLs and the waveguides (typically tens of microns thick by ~ 100 microns wide), the requirement for the strict alignment of a QCL and its waveguide, and a QCL's need for roughly 1 Amp of bias current while being electrically isolated from the gold waveguide walls. Waveguides for THz are usually made by high precision traditional metal machining tools, but the Sandia team recognized that this conventional approach was unsuitable to the integration task and also wanted to make the entire process compatible with semiconductor fabrication methods scalable to mass production. The Sandia strategy was to start with a working QCL device, design a proper waveguide for the QCL using electromagnetic simulation software, and then apply sophisticated semiconductor micromachining methods to build the designed waveguide structure around the QCL.

Sandia's demonstration of a QCL-integrated waveguide clears the way to making THz radiation from QCLs much more widely practical. In the waveguide, the THz electromagnetic field propagation characteristics can be engineered using known waveguide techniques such as couplers (Fig. 3), twists, bends, splitters, and horn antennas. A rectangular waveguide is also the preferred way for mating THz components into larger scale circuits and systems. Ultimately, the Sandia team aims to further integrate a THz detector device with the QCL/waveguide structure and create a compact, microelectronic THz transceiver, which will finally put the THz spectrum on a technological par with microwave electronics and infrared photonics.

Thermal Microphotonic Detection and Imaging
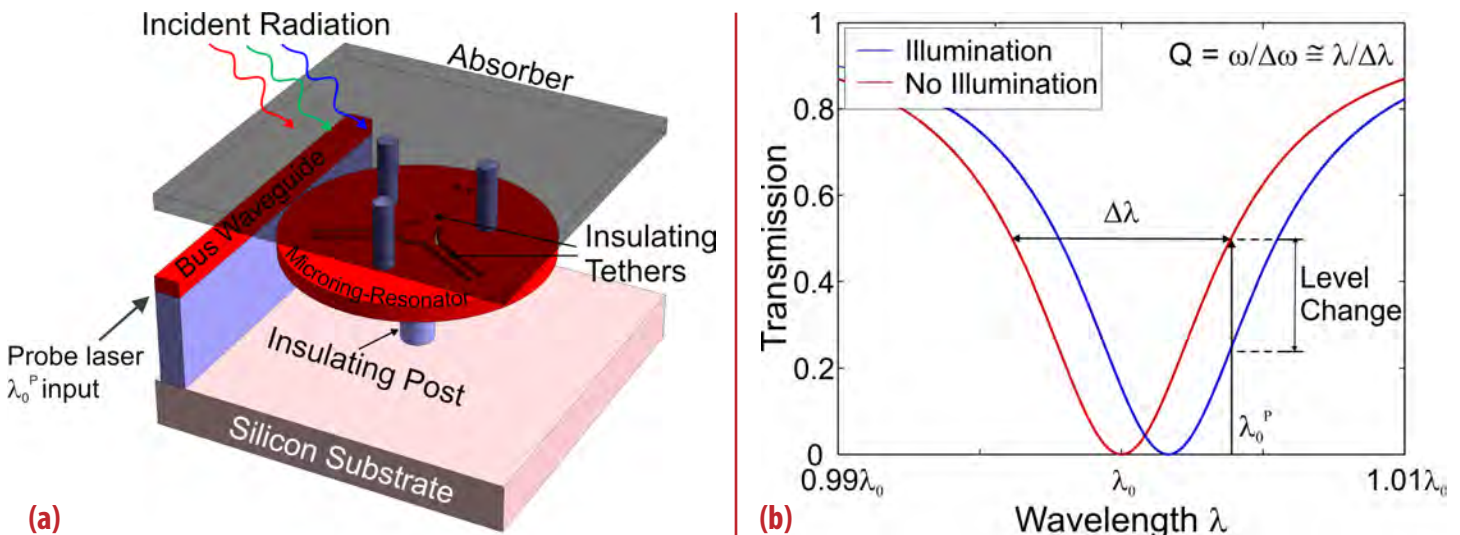
Figure 1: Thermal detection using optical resonators. (a) Schematic of a thermal microphotonic detector, consisting of a thermally isolated resonator thermally coupled to an absorbing element and evanescently coupled to a bus waveguide. (b) Readout consists of an interrogating laser sitting at the 3dB point of the resonance. Upon illumination, the temperature of the microresonator increases, shifting the resonant wavelength via the thermo-optic effect and a level change is sensed.

Optical resonators offer potential for significant improvements in thermal imaging

For more information:
Technical Contact:
Michael R. Watts
505-284-9616
mwatts@sandia.gov

Science Matters Contact:
Alan Burns, Ph.D
505-844-9642
aburns@sandia.gov

Most modern optical imagers, such as focal plane arrays (FPAs), are constructed of arrays of photon detectors. The detectors directly generate electron-hole pairs from the incident radiation and provide excellent noise performance when the photon energy is much larger than the thermal energy k_BT. However, for wavelengths longer than a few microns, photon detectors have to be cooled, often to cryogenic temperatures, in order to minimize thermally-induced transitions. Alternatively, thermal FPAs can be formed from uncooled detectors, where the incident radiation generates thermal energy and a corresponding temperature shift. This shift is then sensed through a change in some physical characteristic (e.g., mechanical, electrical, or optical) of the detector element.

Fundamentally, thermal detectors are limited by thermal phonon fluctuations due to energy exchange with their surroundings. However, the best thermal detectors (i.e. microbolometers), do not reach the thermal phonon fluctuation limit since resistive elements in microbolometers suffer from Johnson noise, $1/f$ noise, and poor thermal isolation.

At Sandia, we are developing uncooled thermal detectors based on microphotonic resonators that offer better noise performance, smaller pixel size (5µm), and faster response times than existing thermal detectors. Thermal microphotonic detection involves combining high-quality-factor- (Q-) micron-scale resonators with extreme thermal isolation to ensure low-noise thermal detection. As shown in Fig. 1a, it consists of a bus waveguide, a thermally-isolated microresonator, and an absorbing element in thermal contact with the microresonator. The absorber converts incident optical power to thermal power, causing a rise in temperature in both the absorber and the resonator. This temperature rise shifts the resonance through the thermo-optic effect, as depicted in Fig. 1b. The shift can be
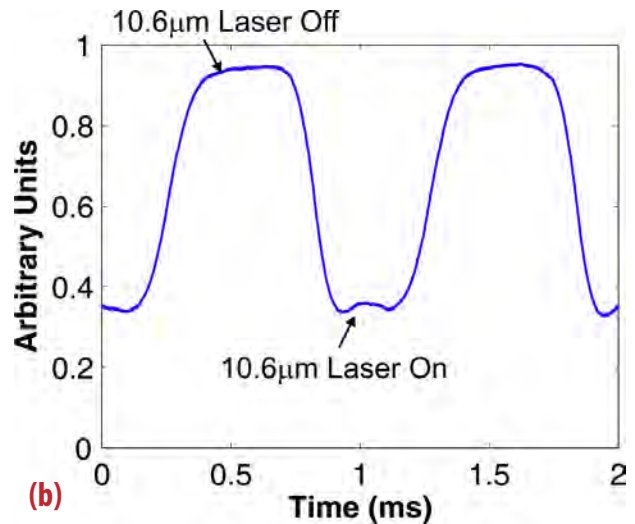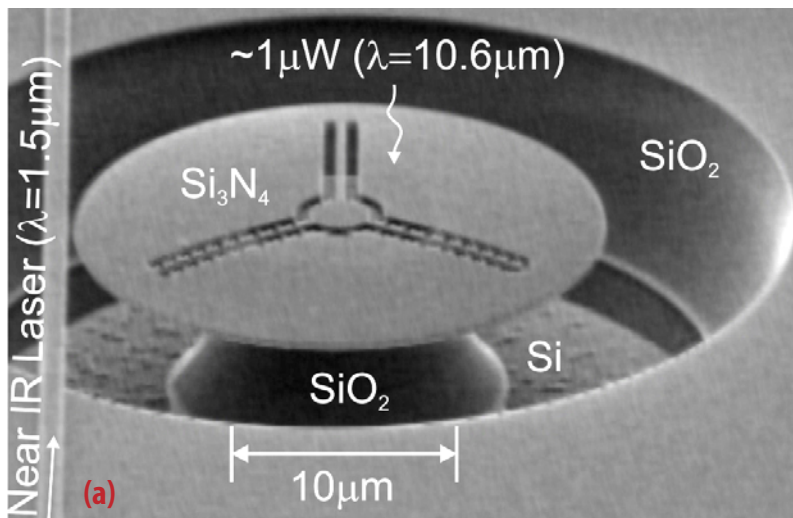
Figure 2: Prototype microphotonic thermal detectors. (a) Scanning electron micrograph of a silicon-nitride-based detector. (b) Resonator response to absorption of chopped 1µW 10.6µm CO_2 laser. The resulting temperature change induces a change in the transmission of the near-infrared ($\lambda = 1.5$µm) laser line interrogating the resonator as described in Fig. 1b.

detected by a laser line operating at one of the 3dB points of the resonance. The very high Q, along with the high degree of thermal isolation that can be achieved by dielectric supports, enables thermal microphotonic detectors to achieve scale factors three-to-four orders of magnitude greater than that achieved with microbolometers. In addition, microphotonic detectors do not suffer from Johnson noise in the sensing element, do not have significant $1/f$ noise components, and are not perturbed by the interrogating signal. All of these traits point to the potential to measure thermal fluctuations two-orders of magnitude below present day microbolometer performance.

Prototype microphotonic detectors have been designed and fabricated at Sandia. A scanning electron micrograph of a detector made of silicon nitride and supported by an oxide post and silicon nitride tethers is presented in Fig. 2a. (Note: The resonator itself is the absorbing element in this prototype). The response to incident thermal radiation (Fig 2b) was obtained by interrogating the 3dB point of the resonance with a near-infrared laser ($\lambda = 1.5$µm) and directly illuminating the absorbing microphotonic resonator with 1µW from a 10.6µm carbon dioxide laser.

Scaling up from a single prototype sensor to a working thermal microphotonic focal plane array (TM-FPA, Fig. 3) will certainly require significant effort. Principal among the challenges is to adopt a scalable and reliable readout approach, such as a wavelength division multiplexed (WDM) readout, whereby an interrogating laser's frequency is scanned to address columns of resonators with different resonant frequencies. If successful, thermal microphotonic detectors

and imagers have the potential to transform uncooled thermal imaging technology, enabling higher sensitivity, higher resolution, and faster response times.
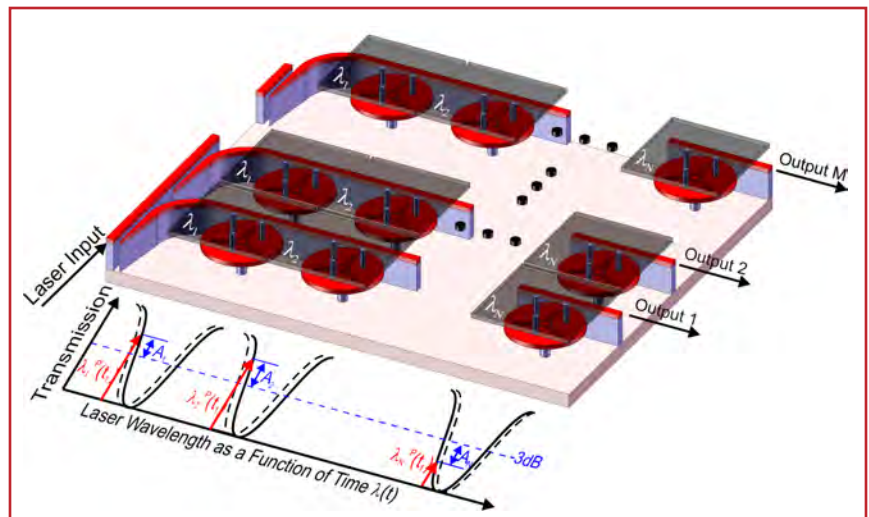

Figure 3: Concept for a TM-FPA, using a WDM-based readout to interrogate columns of sensors. The resonances can be interrogated by simply stepping the laser to a 3dB point of the initial center wavelength of each column and reading out the amplitudes of transmission.

Reference:

M. R. Watts, M. J. Shaw, G. N. Nielson, "Optical resonators: Microphotonic thermal imaging," Nature Photonics, **1**, 632 - 634 (2007)

Microelectronics and Microsystems
Quantum Computing

Silicon Quantum Bits
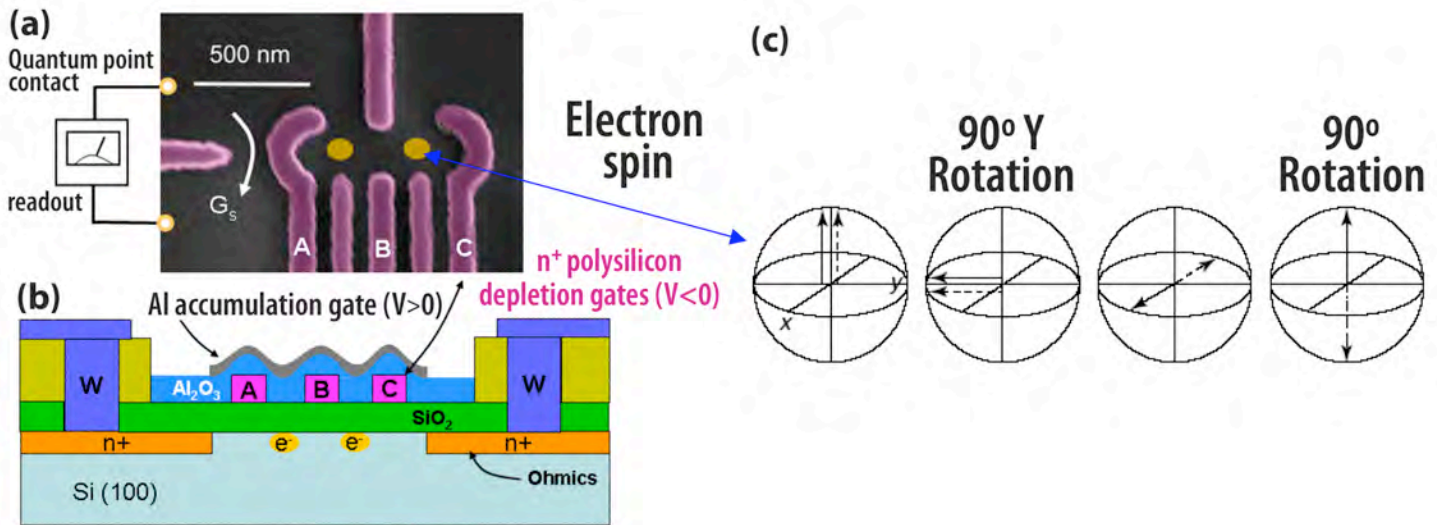
Figure 1: (a) scanning electron microscope image of Sandia's dual quantum dot structure fabricated in silicon (the dots suggest the approximate location of the electron position); (b) schematic cross section of the quantum dot structure showing the position of the single electron locations; and (c) schematic representation of spin manipulation using rotation and precession of two different spins.

Qubit information to be stored in silicon quantum dots

For more information:
Technical Contacts:
Malcolm Carroll
505-284-3499
mscarro@sandia.gov

Thomas Tarman
505-844-4975
TDTarma@sandia.gov

Science Matters Contact:
Alan Burns, Ph.D
505-844-9642
aburns@sandia.gov

The Quantum Information Science and Technology (QIST) Grand Challenge is a three-year research effort aimed at producing the world's first silicon-spin-based quantum bit (qubit). Qubits are the basic information storage elements of quantum computers, which perform quantum information processing and offer the opportunity to efficiently solve problems that are numerically challenging for classical computers. Quantum computers, therefore, may someday augment conventional classical computers by employing some of the unusual properties of quantum systems to speed up computation.

A critical challenge in building a quantum information processing system is the need to couple and manipulate tiny qubits in the form of a quantum circuit that produces a useful function. Sandia researchers are focused on the basic questions related to the feasibility of manufacturing a simple qubit and simple quantum circuits – a task that includes demonstrating a silicon qubit, integrating the qubit with classical CMOS (Complementary Metal Oxide Semiconductor) technology, and designing quantum error correction circuits that are tuned to the physical qubit's unique properties. Sandia's approach (Figure 1) is to physically encode quantum information in the spin state of an electron that is confined in a silicon quantum dot. Although gallium arsenide quantum dots have been demonstrated, quantum dots made from silicon are expected to have longer decoherence times and improved integration with silicon-based classical circuitry. A significant challenge, therefore, is to engineer the Si qubit and the surrounding electronics, and have them all operating at ~ 0.1K (0.1 degrees above absolute zero).

In the first year of this project, Sandia researchers have fabricated silicon nanoelectronic devices with the goal of isolating, measuring and manipulating single electrons (see Figure 1). Similar structures will be integrated with standard microelectronics circuits that are necessary for future quantum circuitry. The Sandia qubit uses gate features as small as 50 nanometers to apply electrical signals that move and trap individual electrons - functions that will be required in the quantum bits of future quantum circuits. Early measurements show dramatic changes in electrical properties (resonances due to single-electron transistor action) that arise from the addition or removal of a single electron from a quantum dot measuring less than 100 nanometer. This is a critical step towards achieving the goal of measuring and manipulating the quantum spin information encoded in single electrons.
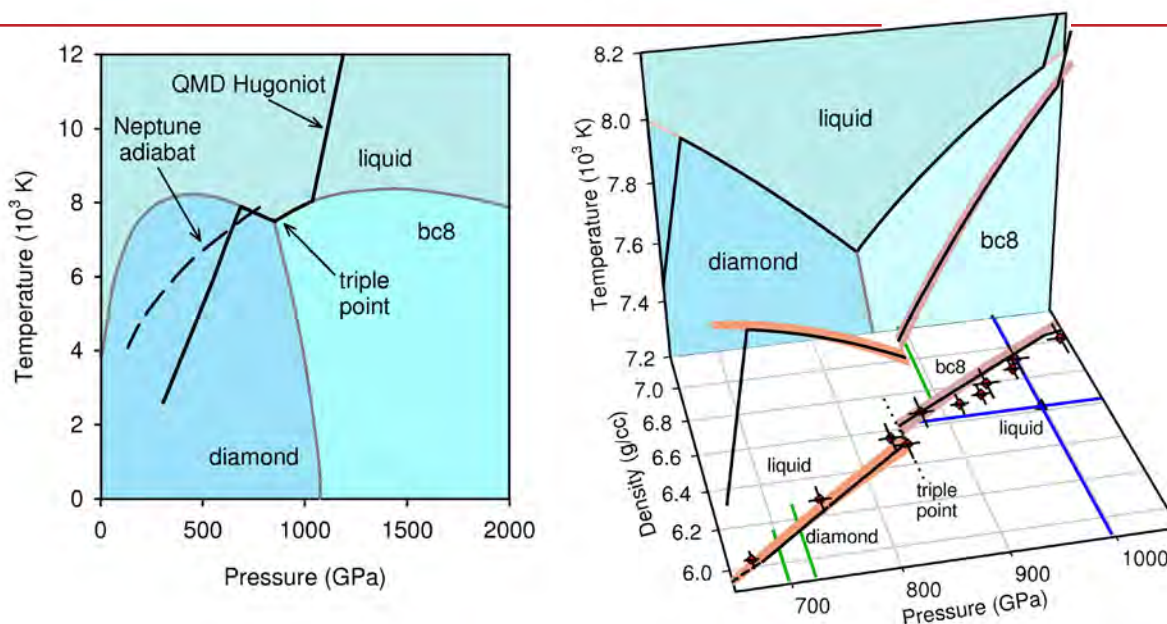
Shock-wave exploration of the high-pressure phases of carbon

Figure 1: (Left) Phase diagram for high energy density carbon. Solid black line, QMD Hugoniot from this work; dashed black line, predicted adiabat for Neptune (Uranus similar). (Right) QMD predictions near the triple point for the diamond-liquid (orange band) and bc8-liquid (magenta band) coexistence regions in density – pressure – temperature space. Also shown are projections in the pressure – temperature (back wall) and pressure – density (floor) planes. The black line is the QMD predicted Hugoniot. The Hugoniot lies within the solid – liquid coexistence over the entire pressure range of ~690 to 1060 GPa, inclusive of the diamond – bc8 – liquid triple point at ~850 GPa. Experimental data are shown in the pressure – density plane; colors and symbols as in Fig. 2.

Melting of diamond under pressure at the Sandia Z machine

For more information:
Technical Contact:
Marcus Knudson
505-845-7796
MDKnuds@sandia.gov

Science Matters Contact:
Alan Burns, Ph.D
505-844-9642
aburns@sandia.gov

Diamond is being considered as one of the ablator materials for inertial confinement fusion (ICF) capsules. Consequently, understanding the melt properties of diamond along the Hugoniot, the locus of end states achievable through compression by large amplitude shock waves, is critical for designing capsules and drive pressure pulse-shapes that minimize the possibility of micro-structural effects during the implosion phase of the capsule; such effects could lead to heterogeneities that would seed instabilities capable of quenching the implosion. In support of the National Ignition Campaign, detailed quantum molecular dynamics (QMD) calculations were performed in the vicinity of the melt transition using the Vienna *ab-initio* simulation package. Concurrently, a series of ultra-high velocity impact experiments were performed at the Sandia Z machine to determine the melt properties of diamond along the Hugoniot.

The QMD calculations predicted the onset and completion of diamond melt along the Hugoniot at pressures of ~690 and ~1060 GPa (6.9 and 10.6 million times atmospheric pressure), respectively (see Fig. 1). Additionally, and possibly more significantly, these calculations also suggested the existence of a diamond-bc8-liquid triple point within the shock melt coexistence region at a pressure of ~850 GPa. As shown in Fig. 2, the resulting Hugoniot near melt exhibits four distinct regions, with significant differences

Sandia National Laboratories

NNSA National Nuclear Security Administration

in shock velocity throughout the coexistence region. However, as seen in Fig. 2a, data obtained from recent experimental studies performed at ultra-intense laser facilities elsewhere were of insufficient accuracy to provide quantitative comparison with these predictions.

A series of 15 flyer plate impact experiments were performed on polycrystalline diamond samples on the Sandia Z machine over the pressure range of 550 to 1400 GPa. The relatively large lateral area of the flyer plates permitted simultaneous loading of three diamond samples, each substantially larger than samples used in previous studies, which enabled precise measurement of the shock wave velocity. Furthermore, measurement of the impact velocity in these experiments enabled precise inference of the particle velocity. These aspects of the experiment enabled roughly an order-of-magnitude improvement in accuracy as compared to recent laser studies, as illustrated in Fig. 2, and enabled quantitative comparison with QMD predictions. These results validate the QMD calculations and provide compelling evidence for the existence of the triple point along the Hugoniot, which is the first experimental evidence of a high-pressure solid phase of carbon beyond that of diamond.

This work dramatically improves the understanding of the melt properties of carbon in this high energy density regime. In addition to being essential in the design of capsules for ICF applications, these data and QMD calculations should also provide for more accurate equation-of-state models for carbon in the regime of interest to planetary physicists. In particular, improved models for carbon may lead to better models for the interiors of Neptune and Uranus that may provide insight into the source of the unusual magnetic fields observed for these two planets.
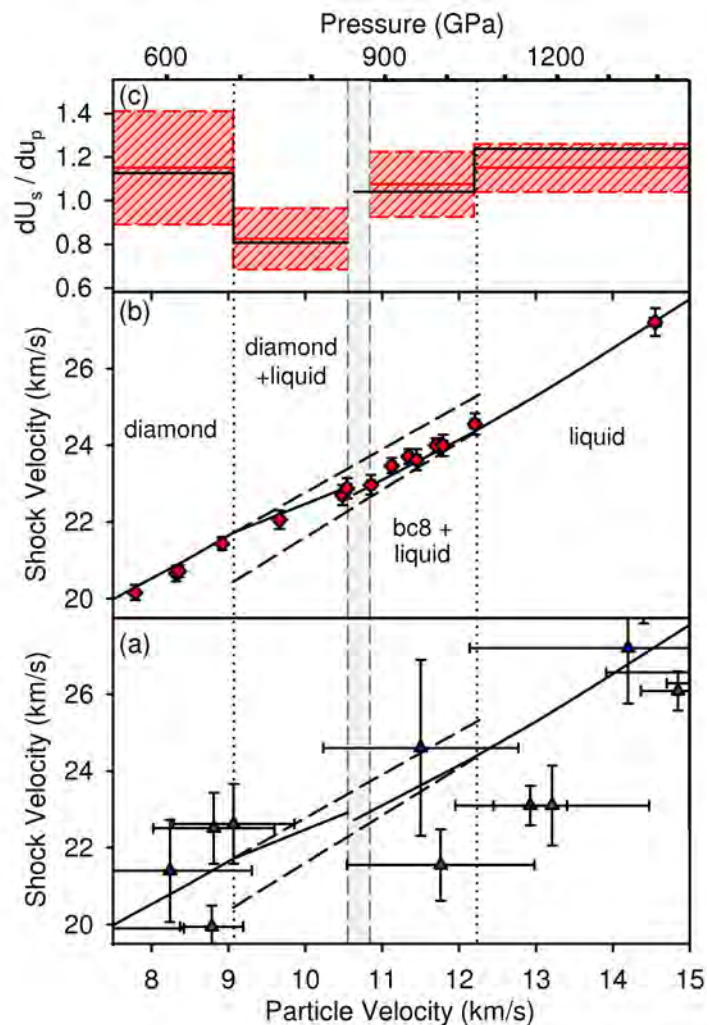
Figure 2: (a) and (b) Diamond Hugoniot in shock velocity, U_s, versus particle velocity, u_p. Solid line, QMD Hugoniot, this work; dashed line, QMD metastable solid and liquid Hugoniots, this work. Experimental data: blue and green triangles, laser driven data; red diamond, this work. (c) Comparison of the U_s-u_p slopes from QMD calculations (solid black line) and a piecewise linear fit to the experimental data (solid red line). Also shown are the uncertainties in the slopes of the fit (dashed red line). Gray region indicates the experimental bounds for the diamond-bc8-liquid triple point.